A Non-Singular Cumulative Damage Model to Predict Fatigue Crack Growth under Service Loading

Jaime Tupiassú Pinho de Castro[1]
Marco Antonio Meggiolaro[1]
Antonio Carlos de Oliveira Miranda[2]
[1]Mechanical Engineering Department, [2]Tecgraf, Computer Graphics Group
Pontifical Catholic University of Rio de Janeiro (PUC-Rio), Brazil

Abstract

After dividing into three classes the mechanisms that can cause load sequence effects on fatigue crack growth depending on where they act in relation to the crack tip (*before*, *at* or *after* it), some results that cannot be explained by plasticity-induced crack closure are discussed. Then, two mechanisms are quantitatively proposed as viable options in these cases, crack bifurcation at the crack tip (studied elsewhere) and damage accumulation ahead of the crack tip. A model of this type is proposed where fatigue cracking is assumed caused by the sequential failure of volume elements or tiny **εN** specimens in front of the crack tip, calculated by damage accumulation concepts. The crack is treated as a sharp notch with a small but not zero radius, avoiding the physically unrealistic singularity at its tip. The crack stress concentration factor and a strain concentration rule are used to calculate the notch root strain and to shift the origin of a modified HRR field, resulting in a non-singular model of the strain distribution ahead of the crack tip. In this way, the damage caused by each load cycle, including the effects of residual stresses, can be calculated at each element ahead of the crack tip using the correct hysteresis loops caused by the loading. This proposed approach is first validated by comparing the measured with the predicted **da/dN**×**ΔK** curves of three structural alloys. The predictions are made using only **εN**, toughness and threshold properties, since the model does not need any fitting constant. This idea is then extended to predict fatigue crack growth under variable amplitude loading, assuming that the width of the volume element broken at each cycle is equal to the region ahead of the crack tip that suffers damage beyond its critical value. The reasonable predictions of the measured fatigue crack growth behavior in steel specimens under service loads corroborate this simple and clear way to correlate **da/dN** and **εN** properties.

1. Introduction

In a classical work, Paris taught us in 1961 that the fatigue crack growth (FCG) rate **da/dN** was controlled by the stress intensity range **ΔK** and not by the stress range **Δσ** applied on the structure. He measured the growth of a fatigue crack in 2 identical cracked aluminum plates subjected to the same **Δσ = ΔP/wt** (where **ΔP** is the force range applied on the plate, **w** is the width and **t** is the thickness of the plate), but had the bright idea of applying **ΔP** on the crack faces in one of the plates and on the plate borders in the other. If the stress range **Δσ** was the controlling factor for the fatigue crack propagation process in those plates, it was expected that their **da/dN** history should be equal (or at least should vary in the same way). But instead the FCG rate **da/dN** increased with the crack length **a** in the plate loaded by its borders, while **da/dN** decreased as the crack grew in the plate loaded by the crack faces. However, when plotting the **da/dN**×**ΔK** curves of both plates they coincided, proving that **ΔK** was the FCG controlling parameter in those tests, see Figure 1 [1-2].

Since Paris' discovery, **ΔK** has been successfully used to predict the fatigue life of cracked structures under constant amplitude loading. But as Miner's rule type calculations turned out to be too conservative in many variable amplitude loading problems, it was early realized that load sequence effects can be very significant in fatigue crack growth problems.

Due to the great practical importance of these problems, fatigue crack growth under real service loading has been a fascinating and challenging research field since the 60's, yet to be completely understood. No one disputes that e.g. an overload (OL) can stop or retard the subsequent fatigue crack growth, but why and how this happens is still far from being a settled issue. There are many who firmly believe that plasticity-induced crack closure [3-4] can explain all such effects [5-6], and many others who are convinced that crack closure cannot be used at all [7-8]. And to make things more interesting, there is plenty of experimental evidence to (at least in part) support both views!

This is no surprise, as there are so many mechanisms that can retard or accelerate the growth of a fatigue crack after significant load amplitude variations [9-11]. These several load interaction mechanisms can act *behind*, *at* or *ahead* of the crack tip, and among them the most important are

- crack closure (*behind* the crack tip), which can be caused by plasticity, oxidation or roughness of the crack faces, or even by strain induced phase transformation, e.g.,
- crack tip blunting, kinking or bifurcation (*at* or close to the crack tip), and
- residual stress and strain fields (*ahead* of the crack tip).

Moreover, these various load interaction mechanisms generally can act simultaneously, with their relative importance in any problem depending on several factors such as crack and piece sizes, dominant stress state at the crack tip, microstructure of the material, mean load, and environment.

Despite some important limitations [7-8, 12-13], plasticity-induced crack closure probably still is the most used mechanism to model and explain load sequence effects in fatigue crack propagation. Fatigue crack closure does occur in real life, and can be measured, e.g., from the slope changes in the compliance (or in the load versus displacement, $\mathbf{P \times \delta}$) curves of predominantly linear elastic cracked structures, as discovered by Elber in the early 70's [3-4] and illustrated in Figure 2 [14]. If plasticity-induced crack closure is the controlling load sequence mechanism, then the expected FCG retardation after an OL can be described as follows (see Figure 3). The OL blunts the fatigue crack tip, suddenly and locally increasing **da/dN** (due to the consequent tip stretching) but, as the crack enters the plastic zone swollen by the overload $\mathbf{zp_{ol}}$, **da/dN** quickly decreases and then slowly increases again until reaching its regular value after the crack crosses $\mathbf{zp_{ol}}$ (regular is the **da/dN** rate at which the crack would be growing in the absence of the OL), as described by von Euw et al. in 1972 [15].

The schematics of the plasticity-induced crack closure or the Elber retardation mechanism in fatigue crack growth after an overload (when the stress intensity range **ΔK**, the plastic zone size **zp** and the crack opening load $\mathbf{K_{op}}$ are elsewhere constant) is illustrated in Figure 4. After crossing the crack tip blunted by the overload, the crack opening load $\mathbf{K_{op}}$ *increases* due to the oversized $\mathbf{zp_{ol}}$ and thus *decreases* the effective stress intensity range $\mathbf{\Delta K_{eff} = K_{max} - K_{op}}$. This decrease in $\mathbf{\Delta K_{eff}}$ would be the reason for the delays on the subsequent crack growth rate, as **da/dN** (supposedly) should depend on $\mathbf{\Delta K_{eff}}$ and not on **ΔK**, since the fatigue crack could grow only after fully opened. In other words, the central arguments of this idea are (i) if the fatigue crack tip is closed it cannot be stretched, and thus cannot grow, and (ii) $\mathbf{K_{op}}$ increases inside $\mathbf{zp_{ol}}$.

This ΔK_{eff} concept has been successfully applied both for design and for analysis in many important variable amplitude loading fatigue problems [11, 16-20], since it can indeed be used to model several experimentally observed load sequence effects in FCG.

E.g., McEvily suppressed overload-induced FCG delays in 12.7mm thick aluminum specimens after symmetrically machining their faces until reaching half of the original thickness, to eliminate the surface increase in closure levels due to the OL (supporting in this way an Elber-controlled retardation mechanism), as illustrated in Figure 5 [21]. Schijve [22] studied the effects of overloads (OLs), OLs followed by underloads (ULs) and of ULs followed by OLs in the fatigue lives of Al 2024-T3 plates, and found a behavior also compatible with elberian crack retardation mechanisms, as shown in Figure 6. The success in explaining the overall fatigue crack growth behavior of these and many other similar problems is probably the reason why there still are scholars and engineers who believe that the Elber mechanism could explain *all* load sequence effects. However, this generalization can be unwise.

Let's avoid at this point the arguments of those who seriously question if plasticity-induced crack closure can be a realistic or a physically admissible model, and let's assume that it at least can be a reasonable phenomenological model to explain many load sequence effects. But even if and when this is the case, assuming that the FCG rate is always controlled by ΔK_{eff} and not by ΔK has some serious consequences not yet as well emphasized as they should be among fatigue designers, as we generally assume that reliable fatigue life predictions can be made (at least for simple loading) by integrating a properly measured $da/dN \times \Delta K$ curve of the material. And these are usually obtained by testing small specimens following a standard procedure.

In practice, the load range ΔP can in principle be measured, and nowadays a proper stress-intensity expression ΔK can be reliably calculated using available numerical tools to solve the stress analysis problem (which depends on ΔP and on the structure and crack geometries) even in non-trivial cases, as illustrated later on. This allows designers to accurately calculate the ΔK load history which is used in integrating the $da/dN \times \Delta K$ curve to predict the structure fatigue life. But if the FCG rate da/dN is really a function of ΔK_{eff} instead of ΔK, one cannot simply *assume* that the da/dN curve measured in the standard specimen was obtained under the same ΔK_{eff} that loads the structure, as in general the stress intensity factor that opens the crack K_{op} and thus ΔK_{eff} do not depend only on ΔK. And there is still no reliable way to calculate K_{op} in complex structures.

Indeed, Newman's classical finite-element calculations of crack opening loads on simple plates [16] showed that ΔK_{eff} has a quite strong dependence on the plate thickness and on the applied σ_{max}/S_{fl} ratio, where $S_{fl} = (S_Y + S_U)/2$ is the so-called flow stress and S_Y and S_U are the yield and ultimate strengths of the material, and σ_{max} is the maximum applied stress.

Therefore, predicting thick plate fatigue lives using $da/dN \times \Delta K$ properties measured by testing thinner specimens could be a *dangerous* practice. In fact, if the fatigue crack growth rate is controlled by ΔK_{eff} instead of by ΔK, generally *unsafe* predictions could be made when using $da/dN \times \Delta K$ data measured under plane stress (plane-σ) conditions to predict the residual life of cracked structures that work under a dominantly plane strain (plane-ε) state. This general assertion is based on the reasonable expectation that crack closure levels in plane-ε are normally *smaller* than in plane-σ. This is a condition that can easily occur in practice if FCG tests made on relatively thin standard specimens are used to predict the life of much thicker structures (a practice, by the way, not forbidden in the ASTM widely used E-647 standard test method for measuring fatigue crack growth rates [23]).

E.g., if $\mathbf{da/dN = A\Delta K^{3.25}}$ is the measured FCG curve under (dominant) plane-σ conditions, and if $\mathbf{\Delta K_{eff,\sigma}}$ and $\mathbf{\Delta K_{eff,\varepsilon}}$ are the Newman's predicted plane-σ and plane-ε effective stress intensity factor ranges shown in Figure 7, the error in plane-ε life predictions based on plane-σ data would depend on the $\mathbf{(\Delta K_{eff,\sigma}/\Delta K_{eff,\varepsilon})^{3.25}}$ ratio, and would be *non*-conservative when $\mathbf{\Delta K_{eff,\sigma} > \Delta K_{eff,\varepsilon}}$.

This quite alarming prediction is illustrated in Figure 8, where it can be seen that thick plate fatigue lives of only 1/5 of the expected lives predicted from the thin plate tests could be obtained in practice. But it should be pointed out that such a strong **da/dN** dependence on the specimen thickness is *not* observed in all cases, as illustrated in Figure 9 [24], indicating that there is still a need for improving the fatigue crack closure modeling procedures.

2. Other Limitations of ΔK_{eff} as a Prediction Tool

Plasticity-induced crack closure is the most popular load sequence effect mechanism, but certainly it is not the only one, as there are several important fatigue problems that cannot be explained by the $\mathbf{\Delta K_{eff}}$ concept. For example, Sadananda and Vasudevan support their strong objections against crack closure using convincing experimental evidence such as fatigue crack growth threshold values $\mathbf{\Delta K_{th}}$ that are higher in vacuum than in air [7-8]. Another important problem that cannot be explained by the Elber mechanism is the crack delays or arrests under high $\mathbf{R = K_{min}/K_{max}}$ ratios, when the minimum value $\mathbf{K_{min}}$ of the applied range $\mathbf{\Delta K = K_{max} - K_{min}}$ always remains *above* $\mathbf{K_{op}}$, the (measured) load that opens the fatigue crack. Experiments presented in Figures 10-13 [13] illustrate this point.

Fatigue crack growth retardation can be clearly observed in Figure 10 after applying 50% overloads ($\mathbf{K_{ol} = 1.5 \cdot K_{max}}$) on a crack growing at a quasi-constant baseline $\mathbf{\Delta K_{bl} = 10MPa\sqrt{m}}$ under a quite high tensile mean load **R = 0.7** in a C(T) specimen of an A-542/2 (2.25Cr1Mo) martensitic steel ($\mathbf{S_Y = 769}$ and $\mathbf{S_U = 838MPa}$, **da/dN×ΔK** curves at **R = 0.05** and at **R = 0.70** presented in Figure 11).

The fatigue test reported in Figure 10 was made under predominantly plane-ε conditions, as both the constant baseline $\mathbf{zp_{bl} \cong 300\mu m}$ and the overload $\mathbf{zp_{ol} \cong 675\mu m}$ plastic zones were smaller than **w/16**, where **w = 12mm** was the specimen thickness (assuming, as usual, that the E-399 [25] plane-ε definition can also be used here, and that $\mathbf{zp \cong (K_{max}/S_Y)^2/2\pi}$). The test frequency was 50Hz, but the OLs were applied at a much smaller 0.1Hz or less, to maintain a close control of the servohydraulic testing machine. The overall crack retardation behavior is very similar to the plane-σ case, but the mechanism that caused it certainly was not plasticity-induced crack closure, as demonstrated in Figure 12. The compliance measurements presented in this figure clearly indicate $\mathbf{K_{op} < K_{min}}$ and $\mathbf{\Delta K_{eff} = \Delta K}$ both *before* and *after* the overload. Therefore, as the fatigue crack was *fully opened* before and after the OL, plasticity-induced variations on $\mathbf{K_{op}}$ cannot be used to justify these load-sequence effects.

It is important to emphasize that these compliance measurements were particularly careful. They were made using a highly sensitive linearity subtractor circuit connected to an analog computer which differentiated its output. These instruments were specially designed and built to enhance the non-linear part of the **P×ε** signal, as reported in [14]. The C(T) back face strain **ε** was a more robust signal than the crack mouth opening displacement **δ** in the tests reported here, but both were used in all the measurements and presented identical results. The $\mathbf{K_{op}}$ measurement uncertainty of this experimental set-up is small, and it can easily detect variations of only 1% in the opening loads. And, by the way, the growth of the fatigue crack could also be easily measured by compliance changes, with a crack increment resolution similar to that obtained in potential drop systems [26].

Figure 13 shows several compliance measurements made before and after *stopping*, by an 100% overload, a crack that was growing at a $\mathbf{\Delta K_{bl} = 10MPa\sqrt{m}}$ and $\mathbf{R = 0.70}$ baseline load. In this case the E399 standard requirement cannot be used to claim dominant plane-ε conditions after the OL (using the estimate $\mathbf{zp \cong (K_{max}/S_Y)^2/2\pi}$, the OL plastic zone was $\mathbf{zp_{ol} \cong w/10}$, whereas the E399 requirement is $\mathbf{zp < w/16}$ for plane-ε). Despite that, no crack closure was again observed before nor after the OL.

Keeping an open mind and avoiding dogmatic arguments (such as "when fatigue crack closure is measured the test is correct, but when it is not the results must obviously be wrong, as closure should always be there"), the only reasonable conclusion is that at a such high $\mathbf{R = 0.7}$ ratio $\mathbf{K_{op}}$ simply was not interfering with the fatigue crack growth process. Moreover, the set of results presented in Figures 15-20 is a still more striking argument against the "plasticity-induced crack closure explaining *all* load interaction effects in FCG" dogma, since in these cases closure was definitely measured before and after the overloads, but $\mathbf{\Delta K_{eff}}$ *increased* in the retardation zone [13].

Figure 15 presents the overall FCG delay obtained after 100% OLs applied on another 12×50mm C(T) of the same 2.25Cr1Mo A-542/2 martensitic steel reported above, tested at a $\mathbf{\Delta K_{bl} = 10MPa\sqrt{m}}$ baseline load, but this time at a much smaller $\mathbf{R = 0.05}$. In this test, the plane-ε conditions were even more clearly dominant, with $\mathbf{zp_{bl} \cong 30\mu m}$ and $\mathbf{zp_{ol} \cong 120\mu m}$ less than 1/100 of the C(T) thickness (assuming again that $\mathbf{zp = (K_{max}/S_Y)^2/2\pi}$). Figure 16 shows the opening loads of this crack measured at the nine cycles preceding the OL (numbered −9 to −1, as the OL cycle was arbitrarily called cycle 0), all obtained using the described setup. It was found that $\mathbf{P_{op}/P_{max} = 0.28}$ in all those tests. Note that the measurements had a very low dispersion, which supports the 1% uncertainty claim made before.

Just after the overload was applied, the closure measurements were repeated and the next eight cycles presented a significantly smaller $\mathbf{P_{op}/P_{max} = 0.23}$ ratio, implying that the OL caused a **22%** ***increase*** in $\mathbf{\Delta K_{eff}}$, as shown in Figure 17. This increase should cause a sudden acceleration of the crack, but even the quite sensitive instrumentation used in this test had no resolution to measure very small crack increments. Despite some claims on the contrary, both potential drop and compliance-based crack length measurements a have a 10-30μm range for their uncertainty as proved in [26], and this is one of the reasons why plane-ε FCG results are not only far less common than those obtained under plane-σ, but also a bit more difficult to judge. Therefore, one cannot conclude from Figure 16 whether in this case occurred the delayed retardation behavior frequently described in plane-σ tests.

However, Figures 18 and 19 present concluding evidence against such a behavior. During the following 10^4 cycles no crack growth was detected either, and the opening load remained *below* its pre-overload value maintaining the $\mathbf{P_{op}/P_{max} = 0.23}$ measured just after the OL. And $7.5 \cdot 10^4$ cycles after the OL, when a small 40μm crack increment had already been detected, the retardation on the FCG rate started to *decrease*, but the crack opening load *increased* to $\mathbf{P_{op}/P_{max} = 0.25}$ and kept increasing (causing, therefore, $\mathbf{\Delta K_{eff}}$ to *decrease*) until reaching its pre-overload $\mathbf{P_{op}/P_{max} = 0.28}$ value at $2.0 \cdot 10^5$ cycles after the OL, when its effect had almost disappeared. In other words, the maximum delay was obtained when the value of $\mathbf{\Delta K_{eff}}$ was minimum, a behavior completely incompatible with an elberian retardation mechanism.

Finally, Figure 20 presents another test where the crack *stopped* after a 200% OL despite a **31%** ***increase*** in $\mathbf{\Delta K_{eff}}$, a result that clearly cannot be explained by the Elber mechanism either. Again this test conditions were clearly plane-ε dominated, as $\mathbf{zp_{ol} \cong w/25}$ in this case and the same type of material and specimen already described was used.

But at least for design purposes it is certainly not sufficient to point out that crack closure cannot explain all load sequence effects observed in fatigue crack propagation. Indeed, it is much more useful to *quantitatively* explore the influence other mechanisms can have on such problems, as discussed later on in this paper. But first some additional comments are made on the use of **ΔK** as a prediction tool in non-trivial variable amplitude load fatigue problems.

3. Fatigue Life Predictions in Complex 2D Structures under Real Loading

Despite all doubts about the mechanisms responsible for the load sequence effects, decent life predictions can nowadays be made even for non-trivial problems such as FCG in complex two-dimensional (2D) structures that work under variable amplitude (VA) loading. This can be achieved by experimentally fitting the parameters of phenomenological or engineering models that describe the overall crack growth behavior, when the FCG law for the material and the **ΔK** expression for the cracked structure are known, as exemplified below.

The generally curved crack path and its associated stress intensity factors (SIF) $\mathbf{K_I}$ and $\mathbf{K_{II}}$ can be efficiently predicted by finite element (FE) procedures. However, the time-consuming remeshing and FE recalculations of the entire structure stress/strain field after each VA event require such a large computer effort that this *global* approach is simply not useful in most practical cases. Moreover, the FE modeling of load sequence effects is, at best, only a partially solved question, and still cannot be reliably used to predict lives in most VA fatigue problems. On the other hand, these problems can be efficiently treated by direct integrating the material **da/dN** law to obtain the crack increment caused by each VA event, considering crack growth retardation or acceleration using semi-empirical design rules. But this *local* approach requires the SIF expression for the crack, usually unknown in real cases.

As the advantages of these two approaches are complementary, the life prediction problem can be successfully divided into two tasks. First, the crack path and its SIF are calculated in a specialized FE program, supposing constant amplitude (CA) loading and using pre-fixed small crack increments and automatic remeshing schemes. An analytical expression $\mathbf{K_I(a)}$ is fitted to the mode I SIF calculated at each crack step, where **a** is the length along the crack path, which then is used in a local approach fatigue program to predict the VA fatigue life. This hybrid (global-local) methodology has been implemented in two specially developed pieces of software named **Quebra** and **ViDa**, and then experimentally validated [27-29].

Quebra is a FE code designed to model cracking problems in arbitrary 2D geometries. This friendly tool is very efficient for automatically remeshing the structure at small discrete crack steps, to predict the generally curved crack path and its $\mathbf{K_I(a)}$ and $\mathbf{K_{II}(a)}$ under simple load. It uses quarter-point special crack tip FE, self-adaptive mesh generation schemes, and 3 reliable crack increment methods: Displacement Correlation, Modified Crack Closure, and J-integral with an Equivalent Domain Integral. To predict the new crack growth direction after each crack step, the **Quebra** user can choose the Maximum Potential Energy Release Rate, or the Minimum Strain Energy Density, or the Maximum Circumferential Stress criterions. **ViDa** was developed to automate fatigue analysis procedures by all the traditional local methods (**SN**, **εN** and weld codes for crack initiation and **da/dN** for crack propagation.) It is particularly useful to deal with complex real loads, considering sequence effects both in the initiation and in the propagation of **1D** and of **2D** (elliptical) cracks, using several counters and filter outputs, corrected hysteresis loops, 2D crack fronts, and extensive databases including properties of more than **13000** materials.

These codes, which can be shared with all groups with joint research programs, are used in the calculations presented in this work. Complete details on these programs are available elsewhere [30].

To verify this hybrid methodology, tests were made on SE(B) and on C(T) specimens, modified with holes designed and machined to curve the crack path. The material was 1020 steel ($\mathbf{S_Y = 285}$ and $\mathbf{S_U = 491MPa}$, $\mathbf{\Delta K_0 = \Delta K_{th}(R = 0) = 11.5}$ and $\mathbf{K_C = 280MPa\sqrt{m}}$, with the **da/dN×ΔK** curves shown in Figure 21). Before the tests, the hole-modified specimens were FE modeled in **Quebra** following the procedures described above, and the hole position was varied in the (numerical) models to obtain the most interesting prediction for the curved crack path, by means of a simple trial-and-error process. After that, the chosen specimen geometries were machined, measured and FE remodeled, to account for small deviations in the manufacturing process.

Even though the curved (but unwarped) crack path geometry is 2D, once it is calculated the crack can be described by its 1D length **a** measured along the crack path. Hence, its $\mathbf{K_I}$ expression can be written as a function of **a**, $\mathbf{K_I(a) = \sigma\sqrt{(\pi a)}\cdot f(a/w)}$. The discrete values of the geometry factors **f(a/w)** were calculated for each crack step in **Quebra** and exported to **ViDa**, where they were automatically fitted by an appropriate continuous analytical function. Then, using this $\mathbf{K_I(a)}$ expressions and the 1020 **da/dN×ΔK** equation, the load program for the test was calculated to maintain a quasi-constant stress-intensity range around $\mathbf{\Delta K_I \approx 20MPa\sqrt{m}}$, with $\mathbf{R = 0.1}$. These values are well within the Paris regime of the 1020 steel, see Figure 21.

Cracks were fatigue propagated in SE(B) specimens with a hole machined to the side of the starting notch. Figure 22 shows a picture of a typical crack path after the test and the FE crack path prediction (made *before* the test) given by the line that connects the open dots in the figure.

Then several modified C(T) specimens were tested, each with a **7mm** diameter hole positioned at a slightly different horizontal **A** and vertical distance **B** from the notch root, see Figure 23. This odd configuration was chosen because two different crack growth behaviors had been predicted by the FE modeling of the holed C(T) specimens, depending on the hole position. The predictions indicated that the fatigue crack was always attracted by the hole, but it could either curve its path and grow toward the hole, or else could be deflected by the hole and continue to propagate after missing it. To test the accuracy of the **Quebra** modeling, the transition point between the "sink in the hole" and the "miss the hole" crack growth behaviors was identified and two borderline specimens were dimensioned: one with the hole only half a millimeter below that point and the other with the hole half a millimeter above it. These specimens were then remodeled to account for machining errors to predict the actual crack path. The measured and the predicted crack paths are compared in Figure 24. Using initial and final (after the simulated FCG) meshes with about 1300/2300 and 2200/5500 elements/nodes, the required computation time in a 500MHz PC was less than 15 minutes.

Two specimens (CT1(CA) and CT2(CA)) were tested under constant and two other under variable amplitude loading, one standard C(T) and the holed specimen CT1(VA). The goals of this experiment were: (i) to check whether the curved crack paths predicted under CA loading would give good estimates for the measured paths under VA; and (ii) to verify if load interaction models calibrated for straight cracks in the standard C(T) could be used to predict the fatigue life of the holed specimen. The VA load histories applied to the tested specimens are shown in Figure 25.

The predicted and measured crack paths for the three modified specimens tested under CA and VA loading are shown in Figure 24. This suggests that the crack path under VA loading is the same as the one predicted under CA.

Therefore, assuming that only the crack growth rate (but not its path) is influenced by load interaction effects, the discussed two-step methodology can be generalized to deal with the VA problem. Thus, the SIF values calculated under CA along the crack path using the **Quebra** program can be exported to the **ViDa** software to predict fatigue life, considering load interaction effects.

To evaluate whether the load interaction models calibrated for straight-crack experiments could also be applied to specimens with curved cracks, several crack retardation models were fitted to the data measured on the standard C(T) data under VA loading. The better results were obtained by the Constant Closure model, where $\mathbf{K_{op}}$ was calibrated as 26% of the maximum overload SIF, $\mathbf{K_{ol,max}}$; by the Modified Wheeler model, with the adjustable exponent estimated as 0.51; and by Newman's closure model (generalized for the VA case), with the stress-state constraint fitted as 1.07 (a value more appropriate to model dominant plane-σ FCG conditions, despite the small **zp**s in this test), see [29] for further details. The measured and fitted growth behaviors are shown in Figure 26.

The fitted parameters were then used to predict the crack growth behavior of the hole-modified CT1(VA) specimen under VA loading, see Figure 27. The significant retardation effects of that test were quite well predicted using these 3 models in the **ViDa** program. In particular, the very simple Modified Wheeler model generated as good a prediction as the more elaborated ones, possibly because its simplistic empirical yield-zone formulation can account for both closure and residual stress effects. These results suggest that many such load interaction engineering models can be used to reasonably predict the crack retardation behavior of curved cracks under VA after being calibrated by testing much simpler straight cracks.

The VA histories in Figure 25 are not identical, but they have similar stress levels and OL ratios. This might be one of the reasons why the same adjustable parameters could be used to describe both tests, as the possible load-spectrum dependency of these parameters might result in poor predictions if completely different VA histories are considered.

In addition, the very high sensitivity of the crack growth predictions with these adjustable parameters is another error source that cannot be ignored. This sensitivity is particularly high when the crack growth rates approach stage I (or near threshold) values, as seen in the post-overload regions with almost horizontal slope in Figures 26 and 27.

In this threshold region, miscalculations of just a few percent for the effective SIF can be the difference between crack growth or crack arrest. Since most life cycles are spent during stage I growth, this is the dominant (and most important) region in fatigue design, where the crack growth rates and load interaction effects should be better modeled and measured.

These points must be carefully considered before generalizing crack retardation experiments made under the Paris regime, where the high fatigue life sensitivity of the with load interaction model parameters is masked by the smaller effect of crack closure or residual stress fields.

Finally, it must be emphasized that the quite reasonable fatigue life predictions shown in Figure 27 were made using 3 engineering models based on *different* mechanistic assumptions. This clearly prove that reasonable fatigue life predictions by no means imply that the supposed mechanism used in the (numerical) load interaction model *caused* the VA sequence effects observed in fatigue tests. It only means that the model is mathematically versatile and can describe the overall crack growth behavior.

And to close this topic, it is worth returning to the justification used to present it. Since plasticity-induced crack closure cannot explain all sequence effects in FCG, it is important to quantitatively explore other possible mechanisms capabilities. Two possible candidates are studied below.

4. Mechanisms That Can Cause Load Sequence Effects Acting *at* the Crack Tip

Crack tip blunting is not an efficient retardation mechanism (because $\mathbf{K_t}$, the stress concentration factor of a blunt fatigue crack, is always very high), but crack branching can be. Overloads can cause crack branching, inducing mixed-mode conditions near to its tip even when the far-field stress is pure traction. Such crack branching can retard or even arrest the subsequent fatigue crack growth behavior because the equivalent SIF $\mathbf{K_b}$ and $\mathbf{K_c}$ of the longer and shorter branches can be considerably smaller than that of a straight crack with the same projected length. Moreover, very small differences between the branch lengths **b** and **c** are enough to cause the shorter branch **c** to arrest as the longer one **b** keeps propagating, in the general case changing its curvature and retarding its growth rate until reaching approximately its pre-OL SIF and growth direction and rate, see Figure 28.

Some analytical solutions have been obtained for the SIF of kinked and branched cracks, but it is very difficult to develop complete analytical solutions to describe their complex propagation behavior. Thus, numerical methods are usually the only practical means to predict the propagation behavior of branched cracks. A summary of such SIF solutions as a function of the deflection angle and the length of the deflected part of the crack is presented in [31]. **Quebra** is an ideal tool to predict the (generally curved) path of a branched crack and to calculate the associated Modes I and II SIF. Its very efficient meshing algorithm is fundamental to avoid elements with poor aspect ratio, since the ratio between the size scale of the larger and smaller elements can be above 1,000 in crack bifurcation calculations.

Details of these calculations, too long to be included here, are available elsewhere [32-35]. But some experimental results are worth mentioning. Figure 29 shows a crack bifurcated by a 100% OL in a 4340 steel specimen. Figure 30 shows the resulting retardation effect of a similar branched crack, which last around 12,600 delay cycles along a process zone of about 0.3mm. Figure 31 shows closure, but $\mathbf{P_{op}}$ remained below $\mathbf{P_{min}}$ before and after the OL. Thus, this is another test where the measured retardation cannot be explained by crack closure. In fact, the bifurcation reduced $\mathbf{P_{op}}$ by 25% due to the increase in the specimen compliance caused by the crack branches. But assuming that crack bifurcation was the dominant growth retardation mechanism, the branching model mentioned above *predicted* a process zone of 307μm and 12,000 delay cycles. In several other tests similar fatigue life predictions were within a factor of two of the measured delay cycles, a quite reasonable result that justifies further research to continue exploring quantitatively the potential of crack branching as a load sequence mechanism.

5. A Non-Singular Critical Damage Model to Quantify What Is Happening *Ahead* of the Crack Tip During the Fatigue Process

Contrary to the laborious modeling of the bifurcation delay mechanism mentioned above, the damage *ahead* of a fatigue crack tip can be estimated using simple but sound hypotheses and standard fatigue calculations. The basic ideas in this modeling process are to suppose that fatigue cracks grow by sequentially breaking small volume elements (VE) ahead of their tips, and that these VE fracture when the crack tip reaches them because accumulate all the damage the material can support. In this way, the so-called **εN** procedures, which are generally used only to model fatigue crack initiation, can be combined with fracture mechanics concepts to predict fatigue crack growth too, using the cyclic properties of the material and the strain distribution ahead of the crack tip. These models can consider the VE width in the FCG direction as being the distance that the crack grows on each cycle, or the FCG rate as being the element width divided by the number of cycles that the crack would need to cross it.

Critical damage models are not new [36-42], but they still need improvements. Most models that assume a singular stress/strain field ahead of the crack tip (concentrating in this way all the damage next to the tip) need some adjustable constant to fit the **da/dN** data, compromising their prediction potential. But the supposed singularity at the crack tip is a characteristic of the mathematical models that postulate a zero radius tip, not of the real cracks, which have a blunt tip when loaded (and finite strains at their tip, or else they would be unstable).

To avoid this problem, the actual finite strain range at the crack tip $\Delta\varepsilon_{tip}$ can be estimated using the stress concentration factor K_t for the blunt crack [43] and a strain concentration rule. The strain range field ahead of the crack tip can then be upper-bounded by $\Delta\varepsilon_{tip}$ (e.g. by assuming $\Delta\varepsilon_{tip}$ constant inside region I in Figure 32, where the singular solution would predict strains greater than $\Delta\varepsilon_{tip}$). Supposing that all fatigue damage occurs inside this region I next to the tip, the number of cycles N^* associated with $\Delta\varepsilon_{tip}$ can be obtained from Coffin-Manson's rule, and the FCG rate **da/dN** can then be estimated as the length of region I divided by N^*. But such models have two shortcomings. First, neglecting the fatigue damage outside region I concentrates it in the few very last N^* cycles, a non-conservative hypothesis. Second, assuming an intermittent (grouped by N^* cycles) and not a cycle-by-cycle FCG, although valid in some cases of crazing in polymers, is certainly not true for most metallic structures, as verified by microscopic observations of fatigue striations.

To avoid these limitations, the model proposed here [40-42] (i) uses Schwalbe's modification [37] of the HRR field [44-46] to represent the strain range distribution ahead of the crack tip, and (ii) removes the crack tip singularity by shifting the origin of the strain field from the crack tip to a point inside the crack, located by matching the tip strain with $\Delta\varepsilon_{tip}$ predicted by a strain concentration rule, such as Neuber [47], Molsky and Glinka [48], or the linear rule [49]. This approach recognizes that the strain range $\Delta\varepsilon(r, \Delta K)$ in an unbroken VE increases and causes damage in each load cycle as the crack tip approaches it, see Figure 33. Therefore, the VE closest to the tip breaks due to the sum of all damages it suffered during the previous load cycles. In this way, the fatigue crack growth rate under constant ΔK is modeled by the sequential failure of identical VE ahead of the crack tip.

This model is then extended to deal with the VA loading case, which has idiosyncrasies that must be treated appropriately. First, the VE that breaks in any given cycle has variable width, which should be calculated by locating the point ahead of the crack tip where the accumulated damage reaches a specified value (e.g. 1.0 when using Miner's rule). Load sequence effects, such as overload-induced crack growth retardation, are associated with hysteresis loop shifts and with mean load effects on the material εN curve, and can be calculated using the powerful numerical tools available in the **ViDa** software [30]. Moreover, this model can recognize an opening load, and thus can separate the cyclic damage from the closure contributions to the crack growth process.

5.1. Constant Amplitude Loading

In every load cycle, each VE ahead of a fatigue crack tip suffers strain hysteresis loops of increasing range as the tip approaches it (Figure 34). It suffers a damage increment that depends on the strain range in that cycle, a function of the distance r_i from the i-th VE to the tip and of the load ΔK_j at that event. The fracture of a VE near the crack tip occurs when its accumulated damage reaches a critical value, quantified e.g. by Miner's rule, $\Sigma n_j/N_j = 1$, where n_j is the number of cycles of the **j**-th load event and N_j is the number of cycles that the piece would last if loaded solely by that event. Therefore, under constant ΔK (or ΔK_{eff}) it can be assumed that the fatigue crack advances a fixed distance δa in every load cycle.

If, for simplicity, the damage outside the cyclic plastic zone zp_c is neglected, there are thus $zp_c/\delta a$ VE ahead of the crack tip at any instant. Since the plastic zone advances with the crack, each new load cycle breaks the VE adjacent to the crack tip, induces an increased strain range in all other unbroken VE (because the crack tip approaches them by δa, Figure 35), and adds a new element to the damage zone. Thus, as each load cycle causes a growth increment, $n_j = 1$. Moreover, since the VE are considered as small εN specimens, they break when:

$$\sum_{i=0}^{zp_c/\delta a} \frac{1}{N(zp_c - i\cdot\delta a)} = \sum_{r_i=0}^{zp_c} \frac{1}{N(r_i)} = 1 \tag{1}$$

where $N(r_i) = N(zp_c - i\cdot\delta a)$, the fatigue life corresponding to the plastic strain range $\Delta\varepsilon_p(r_i)$ acting at a distance r_i from the crack tip, can be calculated using the coefficient ε_c and the exponent c of the plastic part of Coffin-Manson's rule:

$$N(r_i) = \frac{1}{2}\left(\frac{\Delta\varepsilon_p(r_i)}{2\varepsilon_c}\right)^{1/c} \tag{2}$$

where $\Delta\varepsilon_p(r_i)$ in its turn can be described by Schwalbe's [37] modification of the HRR field:

$$\Delta\varepsilon_p(r_i) = \frac{2S_{Yc}}{E}\cdot\left(\frac{zp_c}{r_i}\right)^{\frac{1}{1+h_c}} \tag{3}$$

In the above equation, S_{Yc} is the cyclic yield strength, h_c the Ramberg-Osgood cyclic hardening exponent, and zp_c is the cyclic plastic zone size in plane strain, which can be estimated, e.g., by [41]:

$$zp_c = \frac{(1-2\nu)^2}{4\pi\cdot(1+h_c)}\cdot\left(\frac{\Delta K}{S_{Yc}}\right)^2 \tag{4}$$

where ν is Poisson's coefficient. Therefore, substituting (4) in (3) results in:

$$N(r_i) = \frac{1}{2}\left[\frac{S_{Yc}}{E\varepsilon_c}\cdot\left(\frac{zp_c}{r_i}\right)^{\frac{1}{1+h_c}}\right]^{1/c} \tag{5}$$

The next step is approximating the VE width δa by a differential da at a distance dr ahead of the crack tip and the Miner's summation by an integral, which is easier to deal with:

$$\frac{da}{dN} = \int_0^{zp_c} \frac{dr}{N(r)} \tag{6}$$

The HRR field describes the plastic strains ahead of an idealized crack tip, thus it is singular at $r = 0$. But an infinite strain is physically impossible (which does not mean that singular models are useless, but only that the damage close to the crack tip is not predictable by them). To eliminate this unrealistic strain singularity, the origin of the HRR coordinate system is shifted into the crack by a small distance X, copying Creager and Paris idea [43]. In this case, (3) and (6) become

$$\Delta\varepsilon_p(r+X) = \frac{2S_{Yc}}{E}\cdot\left(\frac{zp_c}{r+X}\right)^{\frac{1}{1+h_c}} \tag{7}$$

$$\frac{da}{dN} = \int_0^{zp_c} \frac{dr}{N(r+X)} \tag{8}$$

To determine X and $N(r+X)$ two paths can be followed. The first uses Creager and Paris' $X = \rho/2$, ρ being the actual crack tip radius, estimated by $\rho = CTOD/2$, thus

$$X = \frac{\rho}{2} = \frac{CTOD}{4} = \frac{K_{max}^2 \cdot (1-2\nu)}{\pi \cdot E \cdot S_{Yc}} \cdot \sqrt{\frac{1}{2(1+h_c)}} \tag{9}$$

The second path is more reasonable. Instead of arbitrating the strain field origin offset, it determines **X** by first calculating the crack (linear elastic) stress concentration factor K_t [43]:

$$K_t = 2\Delta K / (\Delta\sigma_n \cdot \sqrt{\pi\rho}) \tag{10}$$

For any given ΔK and **R** it is possible to calculate ρ and K_t from (9) and (10), and then the strain range $\Delta\varepsilon_{tip}$ at the crack tip using a strain concentration rule. The solution depends on the material stress-strain behavior, which has been assumed parabolic with cyclic strain hardening coefficient H_c and exponent h_c, with a negligible elastic range. The Linear concentration rule is the simplest, resulting in a plastic strain range at the crack tip given by:

$$\Delta\varepsilon_{tip} = \frac{K_t \cdot \Delta\sigma_n}{E} = \frac{2\Delta K}{E\sqrt{\pi \cdot CTOD/2}} \tag{11}$$

Neuber's rule requires solving both the crack tip stress and strain ranges $\Delta\sigma_{tip}$ and $\Delta\varepsilon_{tip}$:

$$\begin{cases} \Delta\sigma_{tip} \cdot \Delta\varepsilon_{tip} = \cdot \dfrac{(K_t \Delta\sigma_n)^2}{E} = \dfrac{8\Delta K^2}{E \cdot \pi \cdot CTOD} \\ \Delta\varepsilon_{tip} = 2\left(\dfrac{\Delta\sigma_{tip}}{2H_c}\right)^{1/h_c} \end{cases} \tag{12}$$

And according to Molsky and Glinka, $\Delta\varepsilon_{tip}$ is calculated by:

$$\begin{cases} \dfrac{2\Delta K^2}{E \cdot \pi \cdot CTOD} = \dfrac{\Delta\sigma_{tip}^2}{4E} + \dfrac{\Delta\sigma_{tip}}{1+h_c} \cdot \left(\dfrac{\Delta\sigma_{tip}}{2H_c}\right)^{1/h_c} \\ \Delta\varepsilon_{tip} = 2\left(\dfrac{\Delta\sigma_{tip}}{2H_c}\right)^{1/h_c} \end{cases} \tag{13}$$

After calculating $\Delta\varepsilon_{tip}$ at the crack tip using one of these rules, the shift **X** of the HRR field origin is obtained from (7) using $r = 0$, resulting in

$$\Delta\varepsilon_{tip} = \frac{2S_{Yc}}{E} \cdot \left(\frac{zp_c}{X}\right)^{\frac{1}{1+h_c}} \Rightarrow X = zp_c \cdot \left(\frac{2S_{Yc}}{E\Delta\varepsilon_{tip}}\right)^{1+h_c} \tag{14}$$

The strain distribution at a distance **r** ahead of the crack tip, $\Delta\varepsilon_p(r + X)$, without the singularity problem at the crack tip, can now be readily obtained from (7) and (14). The fatigue crack propagation rate is then calculated from (8) as:

$$\frac{da}{dN} = \int_0^{zp_c} 2 \cdot \left(\frac{2\varepsilon_c}{\Delta\varepsilon_p(r+X)}\right)^{1/c} dr \tag{15}$$

This prediction was experimentally verified in SAE1020 and API 5L X-60 steels and in a 7075 T6 Al alloy, using (15) to obtain the constant of a McEvily-type **da/dN** equation [21], which describes the **da/dN×ΔK** curves using only one adjustable parameter:

$$\frac{da}{dN} = A[\Delta K - \Delta K_{th}(R)]^2 \left(\frac{K_c}{K_c - [\Delta K/(1-R)]}\right) \tag{16}$$

where K_c and $\Delta K_{th}(R)$ are the material fracture toughness and crack propagation threshold at the load ratio **R**. To guarantee the consistence of this experimental verification, K_c, $\Delta K_{th}(R)$, the **εN** and the **da/dN** data were all obtained by testing proper specimens manufactured from the same stock of the 3 materials, following ASTM standards.

The various **da/dN×ΔK** experimental curves are compared with this simple model predictions in Figures 36-38. Both the shape and the magnitude of the data are quite reasonably reproduced by the model, with the Linear rule generating better predictions probably because the tests were made under predominantly plane-ε conditions. Since no adjustable constant was used in this modeling, it can be concluded that this performance is no coincidence.

But some remarks are required. First, damage beyond zp_c was neglected to simplify the numerical calculations, but as it accumulates at all points ahead of the crack tip, it is wiser to choose the damage origin by numerically testing its influence on **da/dN**, or better by comparing the predictions with crack propagation tests, as done later on. Second, FE calculations [50] indicate that there is a region adjacent to the blunt crack tip with a strain gradient much lower than predicted by the HRR field. The above model does not reproduce such low gradient, nor account for the required stress redistribution due to the coordinate system origin shifting *into* the crack. These shortcomings could be avoided by shifting the origin *away* from the tip by x_2 and assuming the crack-tip strain range $\Delta\varepsilon_{tip}$ constant over the region I of length x_1+x_2 shown in Figures 39 and 40. x_1 can be obtained equating $\Delta\varepsilon_{tip}$ and the HRR-calculated strain range, and the crack-tip stress range $\Delta\sigma_{tip}$ from:

$$\Delta\sigma_{tip} = \Delta\sigma(r = x_1) = 2S_{Yc} \cdot \left(\frac{zp_c}{x_1}\right)^{\frac{h_c}{1+h_c}} = 2S_{Yc} \cdot \left(\frac{E \cdot \Delta\varepsilon_{tip}}{2S_{Yc}}\right)^{h_c} \tag{17}$$

Then, following Irwin's classical idea, the value of the shift x_2 is obtained by integrating the stress field $\sigma(r)$, guaranteeing that the shadowed areas below the curves in Figure 40 are the same:

$$\int_0^{\infty} \Delta\sigma(r)dr = \int_0^{x_1+x_2} \Delta\sigma_{tip}\,dr + \int_{x_1}^{\infty} \Delta\sigma(r)dr \Rightarrow \int_0^{x_1} \Delta\sigma(r)dr = \int_0^{x_1+x_2} \Delta\sigma_{tip}\,dr \tag{18}$$

Since $x_1 < zp_c$, $\Delta\sigma(r)$ in the above integral can be described by the HRR solution, resulting in

$$\int_0^{x_1} 2S_{Yc} \cdot \left(\frac{zp_c}{r}\right)^{\frac{h_c}{1+h_c}} dr = \Delta\sigma_{tip} \cdot x_1 \cdot (1+h_c) = \Delta\sigma_{tip} \cdot (x_1 + x_2) \Rightarrow x_2 = x_1 \cdot h_c \tag{19}$$

These simple tricks generate a more reasonable strain distribution model (Figure 41):

$\Delta\varepsilon(r) = \Delta\varepsilon_{tip}$, $0 \le r \le x_1 + x_2$ (region I) (20)

$$\Delta\varepsilon(r) = \frac{2S_{Yc}}{E} \cdot \left(\frac{zp_c}{r - x_2}\right)^{\frac{1}{1+h_c}}, \; x_1 + x_2 < r \le zp_c + x_2 \text{ (region II, shifted HRR)} \tag{21}$$

$$\Delta\varepsilon(r) \cong \frac{2S_{Yc}}{E} \cdot \sqrt{\frac{zp_c + x_2}{r}} \cdot \left(1 + \nu \frac{r - zp_c}{zp - zp_c}\right), \; zp_c + x_2 < r < zp \text{ (region III, interpolation)} \tag{22}$$

$$\Delta\varepsilon(r) = \frac{\Delta K \cdot (1+\nu)}{\kappa E \sqrt{2\pi(r - zp/2)}}, \; r \ge zp \text{ (region IV, shifted Irwin)} \tag{23}$$

where $\kappa = 1$ for plane stress and $\kappa = 1/(1-2\nu)$ for plane strain, and

$$zp = \frac{1}{\pi\kappa^2} \cdot \left(\frac{K_{max}}{S_{Yc}}\right)^2 \text{ and } zp_c = \frac{1}{4\pi\kappa^2 \cdot (1+h_c)} \cdot \left(\frac{\Delta K}{S_{Yc}}\right)^2 \tag{24}$$

Both CA and VA fatigue crack growth can then be calculated using these equations (20-24), which consider all the damage ahead of the crack tip (inside and outside the cyclic and monotonic plastic zones) and probably provide a more realistic model of the FCG process.

However, as significant elastic stress components act beyond $\mathbf{r = zp_c}$, equations (2), (5) and (15) must be modified to include Coffin-Manson's elastic coefficient $\boldsymbol{\sigma_c}$ and exponent **b**. And in this case it is certainly better to use **εN** equations which can account for the mean load $\boldsymbol{\sigma_m}$ effects on the VE life such as Morrow elastic (25), Morrow elastic-plastic (26) or Smith-Topper-Watson (27):

$$\frac{\Delta\varepsilon}{2} = \frac{\sigma_c - \sigma_m}{E}(2N)^b + \varepsilon_c(2N)^c \tag{25}$$

$$\frac{\Delta\varepsilon}{2} = \frac{\sigma_c - \sigma_m}{E}(2N)^b + \varepsilon_c\left(\frac{\sigma_c - \sigma_m}{\sigma_c}\right)^{c/b}(2N)^c \tag{26}$$

$$\frac{\Delta\varepsilon}{2} = \frac{\sigma_c^2}{E\sigma_{max}}(2N)^{2b} + \frac{\sigma_c\varepsilon_c}{\sigma_{max}}(2N)^{b+c} \tag{27}$$

But the life **N** in these equations cannot be explicitly written as a function of the VE strain range and mean load and thus must be calculated numerically, a programming task that, despite introducing no major conceptual difficulty, is far from trivial [30].

5.2. Variable Amplitude Loading

The **da/dN×ΔK** curve predicted for CA can be used with some load interaction engineering model in the **ViDa** software for VA problems. But the idea here is to *directly* quantify the fatigue damage induced by the VA load considering the crack growth as caused by the sequential fracture of *variable* size VE ahead of the crack tip. Since the Linear strain concentration rule generated better predictions above, it is the only one used here, and as load interaction effects can have a significant importance in FCG, they are modeled by using Morrow elastic equation to describe the VE fatigue life:

$$N(r+X) = \frac{1}{2}\left(\frac{\Delta\varepsilon_p(r+X)}{2\varepsilon_c}\left(1 - \frac{\sigma_m}{\sigma_c}\right)^{-c/b}\right)^{1/c} \tag{28}$$

To account for mean load effects, a modified stress intensity range can be easily implemented for $\mathbf{R > 0}$ to filter the loading cycles that cause no damage by using:

$$\Delta K_{eff} = K_{max} - K_{PR} = \frac{\Delta K}{1 - R} - K_{PR} \tag{29}$$

where $\mathbf{K_{PR}}$ is a propagation threshold that depends on the considered retardation mechanism, such as $\mathbf{K_{op}}$ or $\mathbf{K_{max}}^*$ from the Unified Approach [7-8]. The damage function for each cycle is then:

$$d_i(r + X_i) = \frac{n_i}{N_i(r + X_i)} \tag{30}$$

If the material ahead of the crack is supposed virgin, then its increment $\boldsymbol{\delta a_1}$ caused by the first load event is the value $\mathbf{r = r_1}$ that makes Equation (30) equal to one, therefore:

$$d_1(r_1 + X_1) = 1 \quad \Rightarrow \quad \delta a_1 = r_1 \tag{31}$$

In all subsequent events, the crack increments take into account the damage accumulated by the previous loading, in the same way it was done for the constant loading case. But as the coordinate system moves with the crack, a coordinate transformation of the damage functions is necessary:

$$D_i = \sum_{j=1}^{i} d_j\left(r + \sum_{p=j}^{i-1}\delta a_p\right) \tag{32}$$

Since the distance $\mathbf{r = r_i}$ where the accumulated damage equals one in the **i**-th event is a variable that depends on $\mathbf{\Delta K_i}$ (or $\mathbf{\Delta K_{eff_i}}$) and on the previous loading history, VE of different widths may be broken at the crack tip by this model. This idea is illustrated by the events schematized in Figure 42.

5.3 Results and Discussions

FCG tests under VA loading were performed on API-5L-X52 steel **50×10mm** C(T) specimens, pre-cracked under CA at $\Delta K = 20MPa\sqrt{m}$ until reaching crack sizes $a \cong 12.6mm$. These cracks were measured within **20μm** accuracy by optical methods and by a strain gage bonded at the back face of the C(T) [26]. The basic monotonic and cyclic properties, measured in computer-controlled servo-hydraulic machines using standard ASTM testing procedures, are $E = 200 \cdot 10^3$, $S_U = 527$, $S_Y = 430$, $S_{Yc} = 370$, $H_c = 840$, and $\sigma_c = 720$ (all in MPa), $h_c = 0.132$, $\varepsilon_c = 0.31$, $b = -0.076$ and $c = -0.53$. About 50 specimens were tested under deformation ratios varying from $R = -1$ to $R = 0.8$ (at least 2 at each strain range) to obtain the **εN** curve, see Figure 43. Morrow's strain-life equation (25), which includes the mean stress effect only in Coffin-Manson's elastic term, best fit the experimental data. The basic **da/dN** curve, measured using the same equipment, is fitted by $da/dN(R = 0.1) = 2 \cdot 10^{-10}(\Delta K - 8)^{2.4}$ (in **m/cycle**), where $\Delta K_{th}(R = 0.1) = 8MPa\sqrt{m}$.

FCG tests were then conducted under several VA histories. The history shown in Figure 44 has 50,000 blocks containing 100 reversals each. The high mean stress levels were chosen to avoid crack closure effects. The load history was counted by the sequential rain-flow method, using the **ViDa** software [30]. The damage calculation was made using a specially developed code following all the procedures discussed above. The crack growth predictions based solely on **εN** parameters are again quite reasonable, see Figure 45. The prediction assuming no damage outside the cyclic plastic zone zp_c underestimated the crack growth. However, when the small (but significant) damage in the material between the cyclic and monotonic plastic zone borders is also included in the calculations, an even better agreement is obtained. Note also that crack growth is slightly underestimated after $1.8 \cdot 10^6$ cycles, probably due to having neglected the elastic damage and the (small) mean stress effects.

A similar test was conducted on AISI 1020 steel C(T) specimen of the same dimensions described above. The measured monotonic and cyclic material properties are $E = 205GPa$, $S_U = 491$, $S_Y = 285$, $S_{Yc} = 270$, $H_c = 941$ and $\sigma_c = 815MPa$, $h_c = 0.18$, $\varepsilon_c = 0.25$, $b = -0.114$, and $c = -0.54$. The FCG curve fit is $da/dN = 5 \cdot 10^{-10} \cdot (\Delta K - \Delta K_{th})^2 \cdot \{K_c/[K_c - \Delta K/(1 - R)]\}$, where $\Delta K_{th} = 11.6$ and $K_c = 277$ (ΔK, ΔK_{th} and K_c in $MPa\sqrt{m}$ and **da/dN** in **m/cycle**).

The VA load history is a series of blocks containing 101 peaks and valleys, as shown in Figure 46, with a duration of two seconds each. Figure 47 compares the predictions with the experimentally obtained data. This other prediction of fatigue crack growth under VA based only on εN properties turns out to be again quite accurate. Therefore, these tests indicate that the ideas behind the proposed critical damage model make sense and deserve to be better explored.

6. Conclusions

Several mechanisms can cause load sequence effects on fatigue crack growth, and they may act *before*, *at* or *after* the crack tip. Plasticity-induced crack closure is the most popular of them, but it cannot explain sequence effects in various important problems. A damage accumulation model ahead of the crack tip based on εN cyclic properties, which can explain those effects in the absence of closure, was proposed for predicting fatigue crack propagation under variable amplitude loading. The model treats the crack as a sharp notch with a small but finite radius to avoid singularity problems, and calculates damage accumulation explicitly at each load cycle. Experimental results show a good agreement between measured crack growth both under constant and variable amplitude loading and the predictions based purely on εN data.

References

[1] Paris PC, Gomez MP, Anderson WE. A Rational Analytic Theory of Fatigue. The Trend in Engineering 1961;13:9-14

[2] Paris PC, Erdogan F. A Critical Analysis of Crack Propagation Laws. Journal of Basic Engineering 1963;85:528-534

[3] Elber W. Fatigue Crack Closure under Cyclic Tension. Engineering Fracture Mechanics 1970;2:37-45

[4] Elber W. The Significance of Fatigue Crack Closure. ASTM STP 486, 1971:230-242

[5] Newman Jr JC. An Evaluation of the Plasticity-Induced Crack-Closure Concept and Measurement Methods. NASA/TM-1998-208430, Langley Research Center, Hampton, Virginia, August 1998

[6] McEvily AJ, Ishihara S. On the development of crack closure at high R levels after an overload. Fatigue and Fracture of Engineering Materials and Structures, 2002;25:993-998

[7] Sadananda K, Vasudevan AK, Holtz RL. Extension of the Unified Approach to Fatigue Crack Growth to Environmental Interactions. International Journal of Fatigue 2001;23:S277-S286

[8] Sadananda K, Vasudevan AK. Fatigue Crack Growth Mechanisms in Steels. International Journal of Fatigue 2003;25:899-914

[9] Suresh S. Fatigue of Materials, 2nd Edition, Cambridge 1998

[10] Skorupa M. Load Interaction Effects During Fatigue Crack Growth under Variable Amplitude Loading - a Literature Review - Part I: Empirical Trends. Fatigue and Fracture of Engineering Materials and Structures 1998;21:987-1006

[11] Skorupa M. Load Interaction Effects During Fatigue Crack Growth under Variable Amplitude Loading - a Literature Review - Part II: Qualitative Interpretation. Fatigue and Fracture of Engineering Materials and Structures 1999;22:905-926

[12] Castro JTP, Parks DM. Decrease in Closure and Delay of Fatigue Crack Growth in Plane Strain. Scripta Metallurgica 1982;16:1443-1445

[13] Meggiolaro MA, Castro JTP. On the Dominant Role of Crack Closure on Fatigue Crack Growth Modeling. International Journal of Fatigue 2003;25:843-854

[14] Castro JTP. A Circuit to Measure Crack Closure. Experimental Techniques 1993;17:23-25

[15] von Euw EFG, Hertzberg RW, Roberts R. Delay Effects in Fatigue Crack Propagation. ASTM STP 513, 1972:230-259

[16] Newman JC. A Crack Opening Stress Equation for Fatigue Crack Growth. International Journal of Fracture 1984;24:R131-R135

[17] DuQuesnay DL, Topper TH, Yu MT, Pompetzki M. The Effective Stress Range as a Mean Stress Parameter. International Journal of Fatigue 1992;14:45-50

[18] Paris PC, Tada H, Donald ‚JK. Service Load Fatigue Damage - a Historical Perspective. International Journal of Fatigue 1999;21:S35-S46

[19] Kujawski D. Enhanced Model of Partial Crack Closure for Correlation of R-ratio Effects in Aluminum Alloys. International Journal of Fatigue 2001;23:95-102

[20] Bunch ,JO, Trammell R, Tanouye P. Structural Life Analysis Methods Used on the B-2 Bomber. ASTM STP 1292, 1996:220-247

[21] McEvily AJ. Current Aspects of Fatigue. Metal Science 1977;11:274-284

[22] Schijve J. Fatigue of Structures and Materials, Kluwer 2001

[23] ASTM Standard E 647. Standard Test Method for Measurement of Fatigue Crack Growth Rates. ASTM Standards;03.01

[24] Ruckert COFT, Tarpani JR, Milan MT, Bose WW, Spinelli D. Evaluating the Berkovitz's K-Parametrization Method to Predict Fatigue Loads in Failure Investigations. 2nd SAE Brazil International Conference on Fatigue 2004, in CD-ROM

[25] ASTM Standard E 399. Standard Test Method for Plane-Strain Fracture Toughness of Metallic Materials. ASTM Standards;03.01

[26] Castro JTP. Some Critical Remarks on the Use of Potential Drop and Compliance Systems to Measure Crack Growth in Fatigue Experiments. Brazilian Journal of Mechanical Sciences 1985;7:291-314

[27] Miranda ACO, Meggiolaro MA, Castro JTP, Martha LF, Bittencourt TN. Fatigue Crack Propagation under Complex Loading in Arbitrary 2D Geometries. ASTM STP 1411, 2002:120-145

[28] Miranda ACO, Meggiolaro MA, Martha LF, Castro JTP, Bittencourt TN. Prediction of Fatigue Life and Crack Path in Generic 2D Structural Components. Engineering Fracture Mechanics 2003;70:1259-1279

[29] Miranda ACO, Meggiolaro MA, Castro JTP, Martha LF. Fatigue Life Prediction of Complex 2D Components under Mixed-Mode Variable Loading. International Journal of Fatigue 2003;25:1157-1167

[30] www.tecgraf.puc-rio.br/vida

[31] Suresh S, Shih CF. Plastic Near-tip Fields for Branched Cracks. International Journal of Fracture 1986;30:237-259

[32] Meggiolaro MA, Miranda ACO, Castro JTP, Martha LF. Numerical Prediction of the Propagation of Branched Fatigue Cracks", in Computational Fluid and Solid Mechanics II, Elsevier 2003:432-435

[33] Miranda ACO, Meggiolaro MA, Castro JTP, Martha LF. Finite Element Modeling of Fatigue Crack Bifurcation. Computational Fluid and Solid Mechanics II, Elsevier 2003: 460-463

[34] Miranda ACO, Meggiolaro MA, Castro JTP, Martha LF. Quantitative Evaluation of Fatigue Crack Growth Retardation Due to Crack Branching. 2nd SAE Brazil International Conference on Fatigue, São Paulo, SP, SAE # 2004-01-2218, 2004, in CD-ROM

[35] Miranda ACO, Meggiolaro MA, Castro JTP, Martha LF. Crack Retardation Equations for the Propagation of Branched Fatigue Cracks. Submitted to International Journal of Fatigue

[36] Majumdar S, Morrow J. Correlation Between Fatigue Crack Propagation and Low Cycle Fatigue Properties. ASTM STP 559, 1974:159-182

[37] Schwalbe KH. Comparison of Several Fatigue Crack Propagation Laws with Experimental Results. Engineering Fracture Mechanics 1974;6:325-41

[38] Glinka G. A Cumulative Model of Fatigue Crack Growth. International Journal of Fatigue 1982;4:59-67

[39] Glinka G. A Notch Stress-Strain Analysis Approach to Fatigue Crack Growth. Engineering Fracture Mechanics 1985;21:245-61

[40] Castro JTP, Kenedi PP. Prediction of Fatigue Crack Propagation Rates Departing from Coffin-Manson Concepts. Journal of the Brazilian Society of Mechanical Sciences, 1995;17(3):292-303 (in Portuguese)

[41] Durán JAR, Castro JTP, Payão Filho JC. Fatigue Crack Propagation Prediction by Cyclic Plasticity Damage Accumulation Models. Fatigue and Fracture of Engineering Materials and Structures 2003;26:137-50

[42] Durán JAR, Castro JTP, Meggiolaro MA. A Damage Accumulation Model to Predict Fatigue Crack Growth under Variable Amplitude Loading Using εN Parameters. Fatigue 2002, Emas 2002:2759-76

[43] Creager M, Paris PC. Elastic Field Equations for Blunt Cracks with Reference to Stress Corrosion Cracking. International Journal of Fracture Mechanics 1967;3:247-52

[44] Hutchinson JW. Singular Behavior at the End of a Tensile Crack in a Hardening Material. Journal of the Mechanics and Physics of Solids 1968;16:13-31

[45] Rice JR, Rosengren GF. Plane Strain Deformation Near a Crack Tip in a Power Law Hardening Material. Journal of the Mechanics and Physics of Solids 1968;16:1-12

[46] Hutchinson JW. Nonlinear Fracture Mechanics. Tech. University of Denmark 1979

[47] Neuber H. Theory of Stress Concentration for Shear-Strained Prismatical Bodies with an Arbitrary Non-Linear Stress-Strain Law. Journal of Applied Mechanics 1961;28:544-551

[48] Molsky K, Glinka G. A Method of Elastic-Plastic and Strain Calculation at a Notch Root. Materials Science and Engineering 1981;50:93-100

[49] Stephens RI, Fatemi A, Stephens RR, Fuchs HO. Metal Fatigue in Engineering. Interscience 2000

[50] Parton VZ, Morozov EM. Elastic-Plastic Fracture Mechanics. Mir Publishers, Moscow, 1978

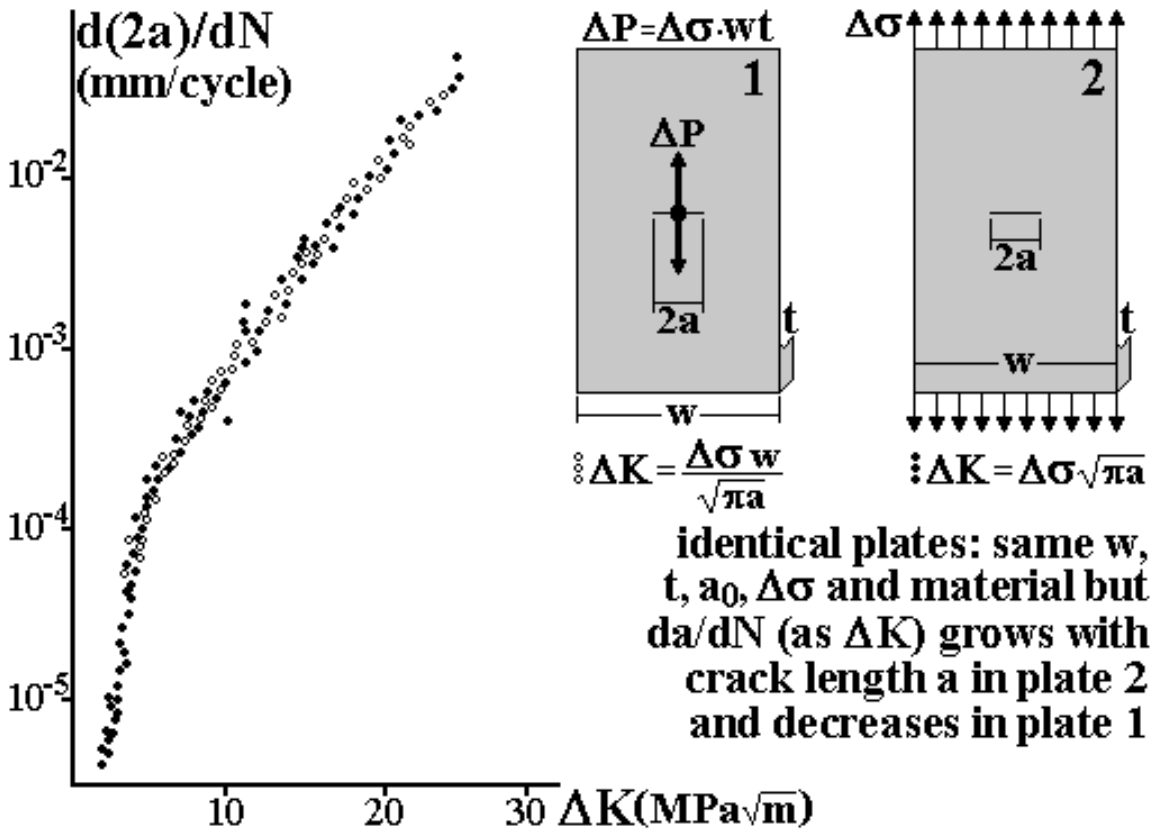

Figure 1: Paris' classical experiment which proved that the fatigue crack growth controlling parameter was the stress intensity range **ΔK**, not the stress range **Δσ** [2].

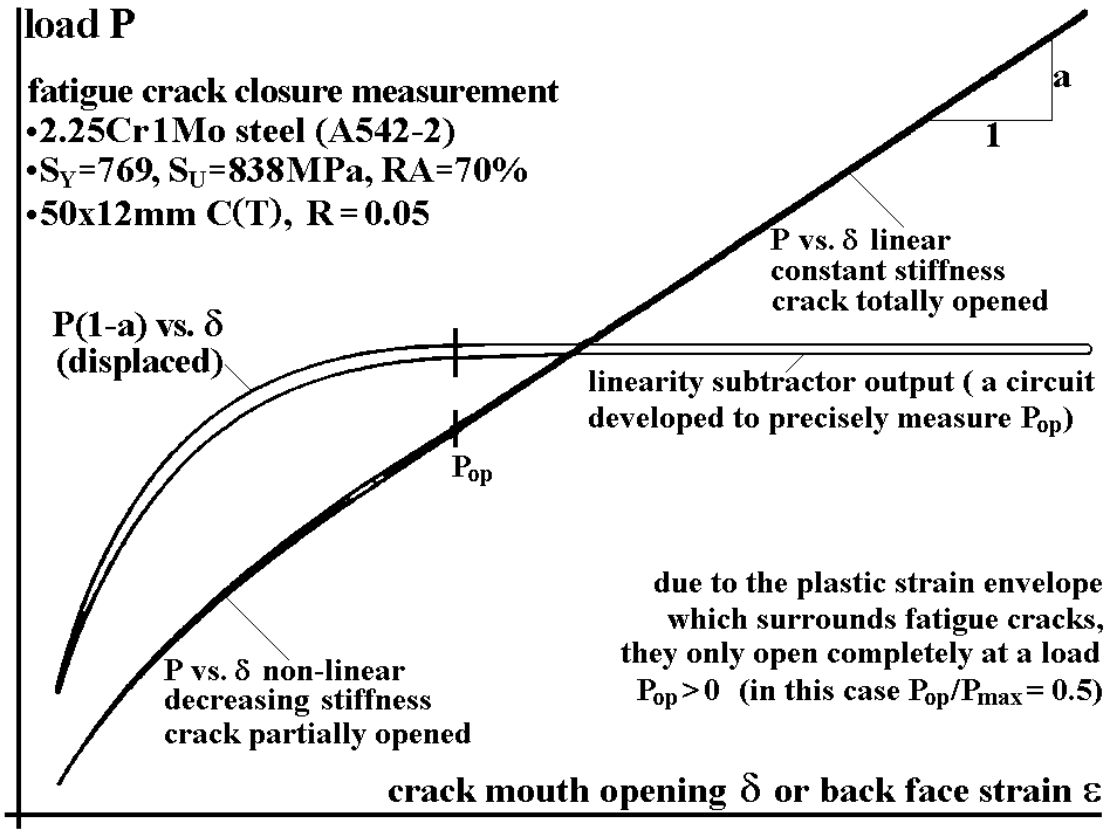

Figure 2: Typical crack closure measurement, where the non-linear part of the **P×δ** curve is enhanced by a technique called linearity-subtraction [14].

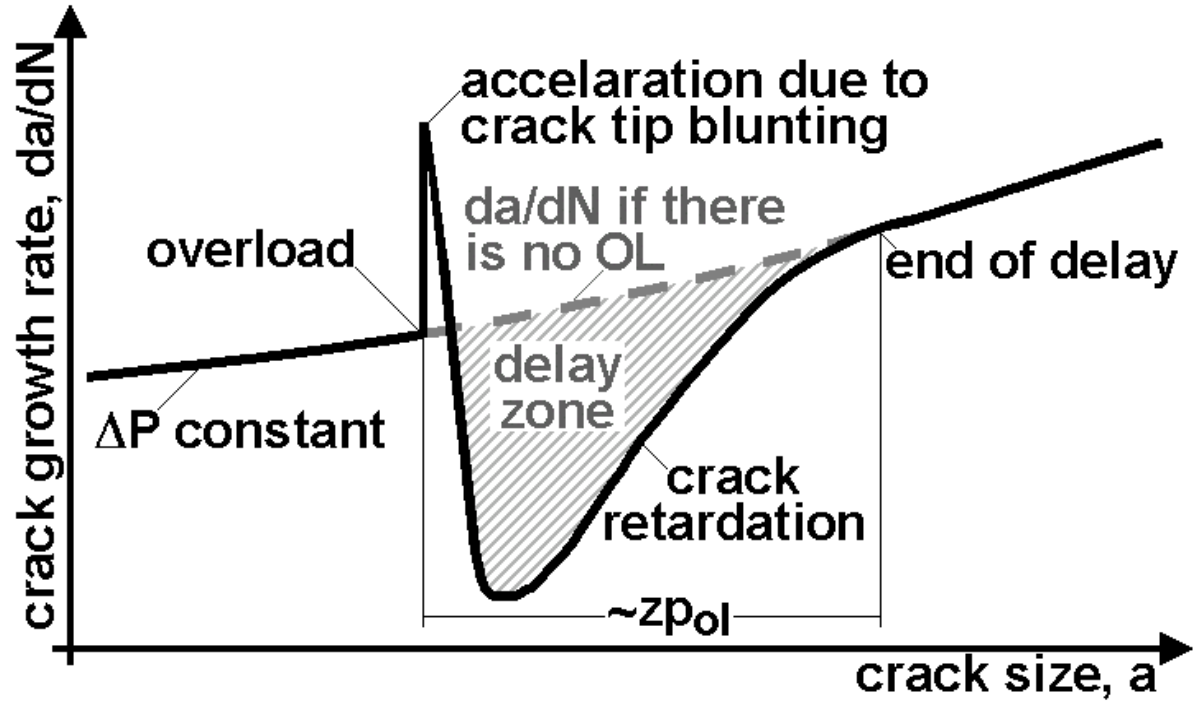

Figure 3: Expected fatigue crack growth retardation after an overload due to plasticity-induced crack closure [15].

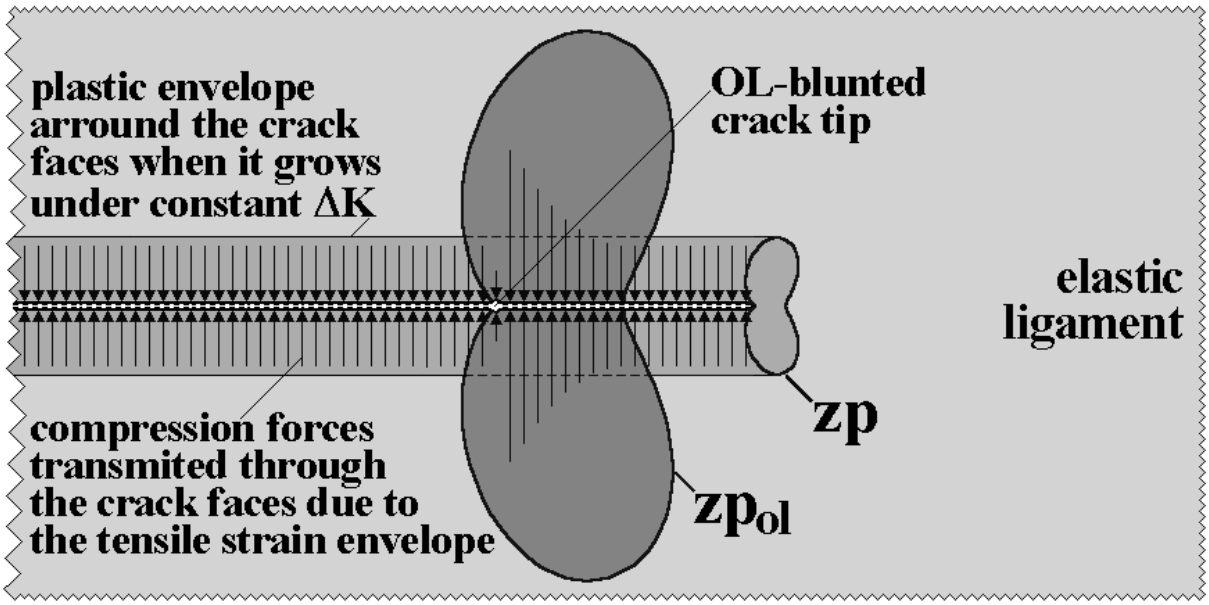

Figure 4: Schematics of the plasticity-induced crack closure (or the Elber [3-4]) retardation mechanism after an overload when **ΔK** is elsewhere constant.

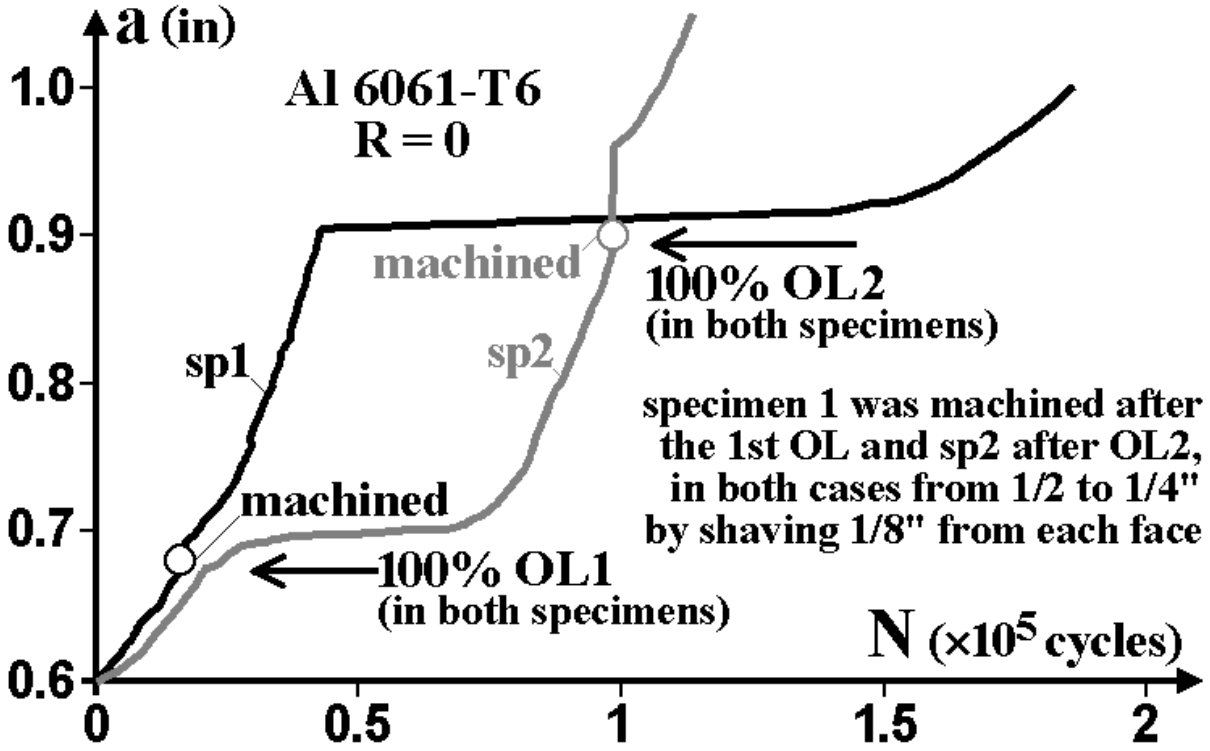

Figure 5: McEvily's measured crack lengths, who avoided overload-induced FCG delays in 12.7mm thick Al specimen by machining their faces until half the original thickness to eliminate the surface closure (supporting an Elber-controlled retardation mechanism) [21].

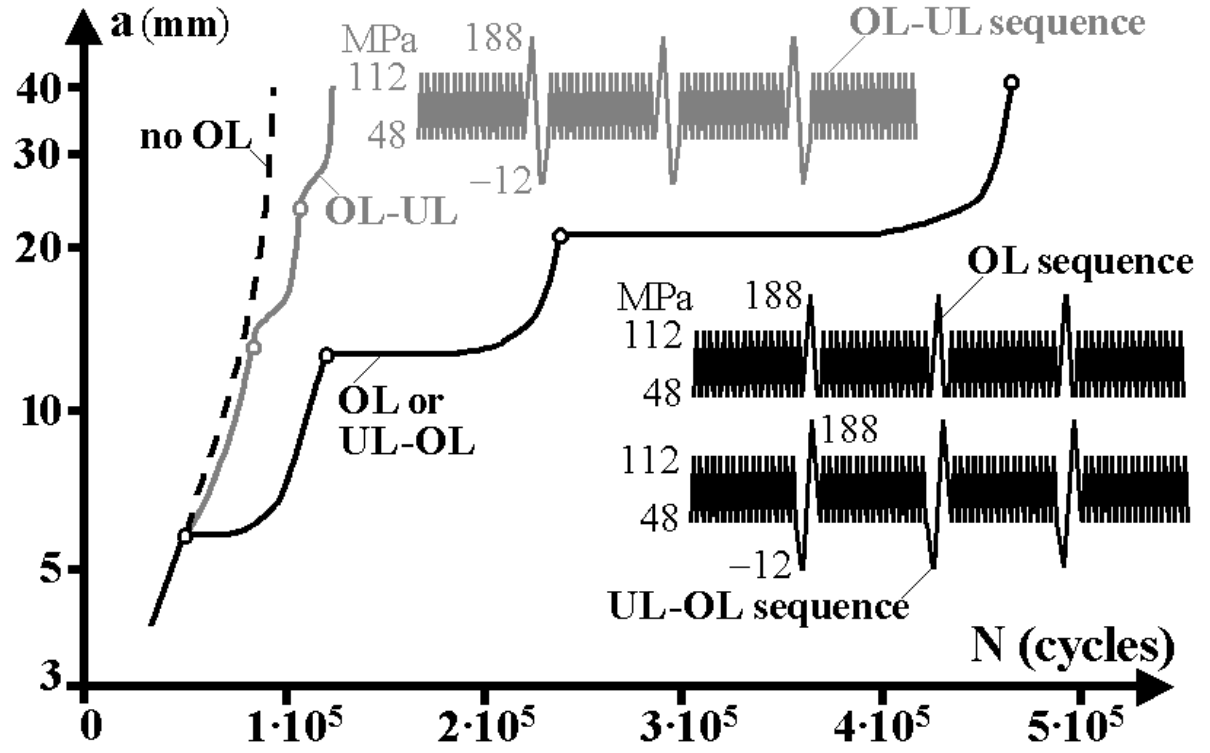

Figure 6: Effect of overloads (OLs), OLs followed by underloads (UL) and of ULs followed by OLs in Al 2024-T3 plate lives reported by Schijve, a behavior also compatible with elberian mechanisms [22].

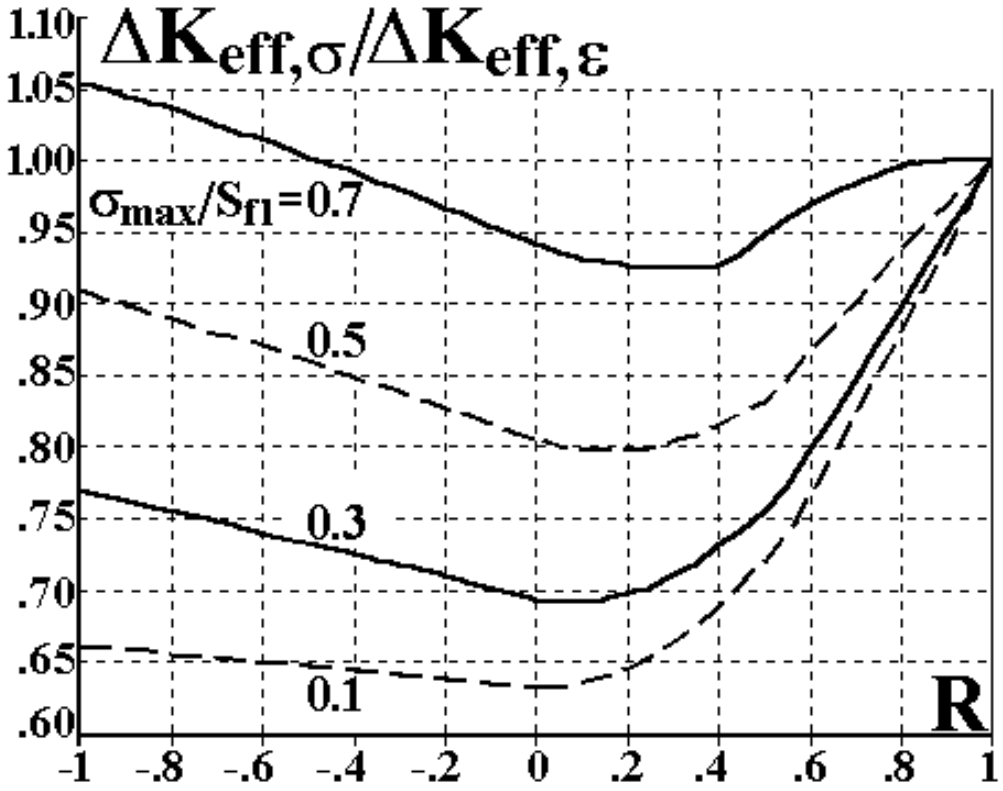

Figure 7: Ratio $\Delta K_{eff,\sigma}/\Delta K_{eff,\varepsilon}$, which could be much smaller than one according to Newman's finite element based calculations of the opening loads in plates [16].

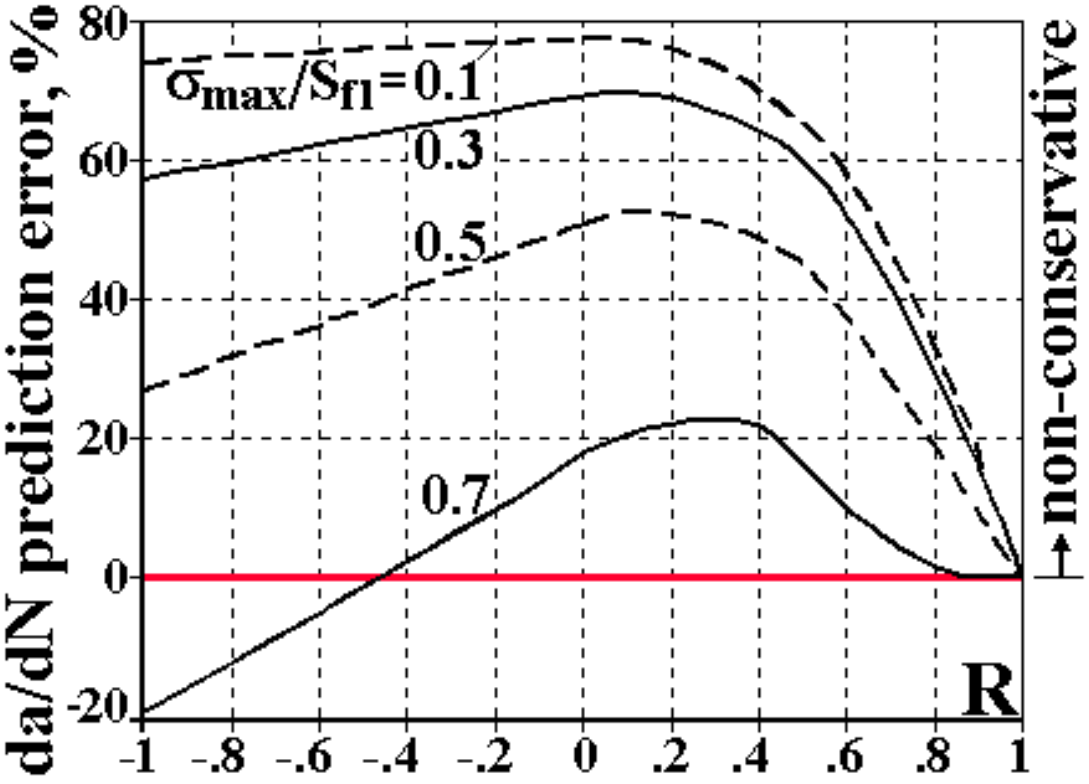

Figure 8: ***Non-conservative*** plane-ε fatigue life predictions obtained by using a $\mathbf{da/dN = A\Delta K^{3.25}}$ FCG curve measured under plane-σ conditions, assuming Newman's $\Delta K_{eff,\sigma}/\Delta K_{eff,\varepsilon}$ expressions.

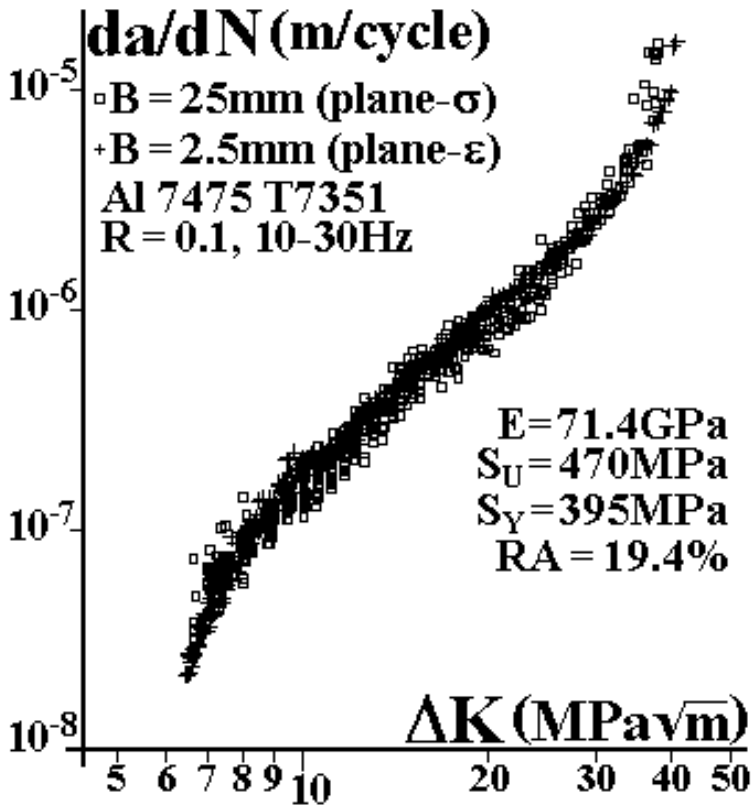

Figure 9: This **da/dN×ΔK** data measured in **2.5** and **25mm** thick specimens of Al 7475, under plane-σ and plane-ε dominated conditions respectively [24], shows no dependence in the thickness, supporting in this way the ASTM standard that does not forbid the use of thin specimens to measure the FCG behavior of a given material.

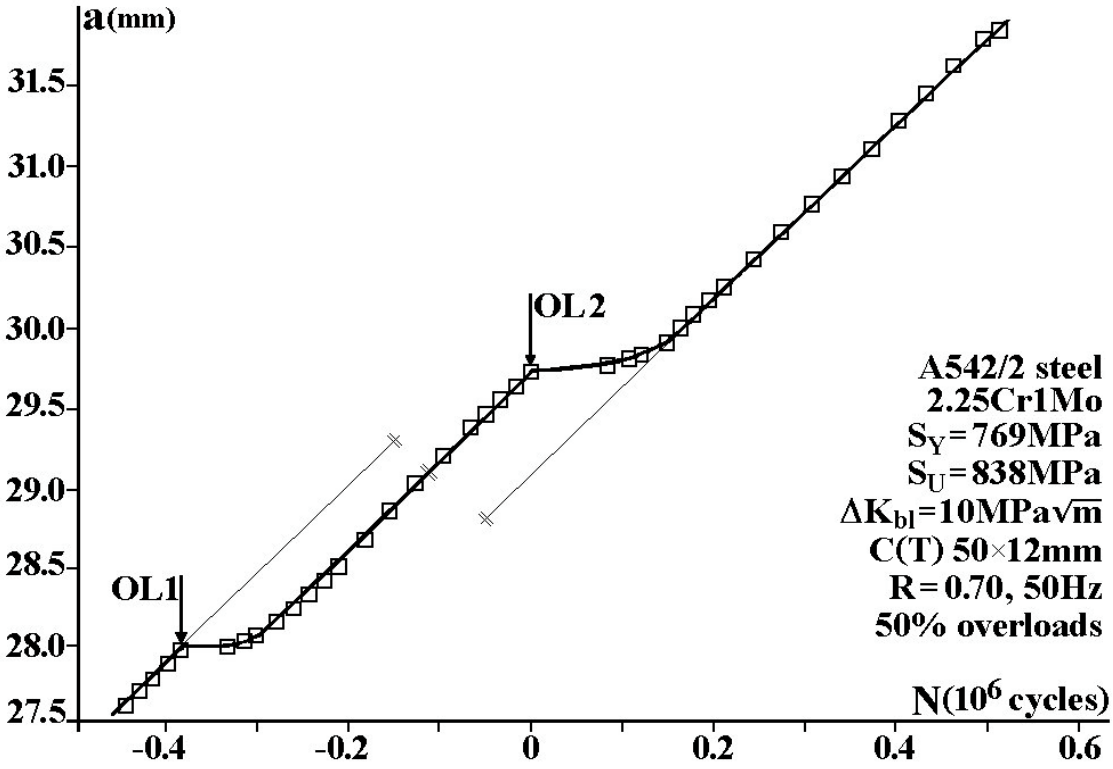

Figure 10: Fatigue crack growth retardation after **50%** overloads applied at a high **R = 0.7**, on a crack growing at a quasi-constant ΔK_{bl} **= 10MPa√m** under plane-ε conditions.

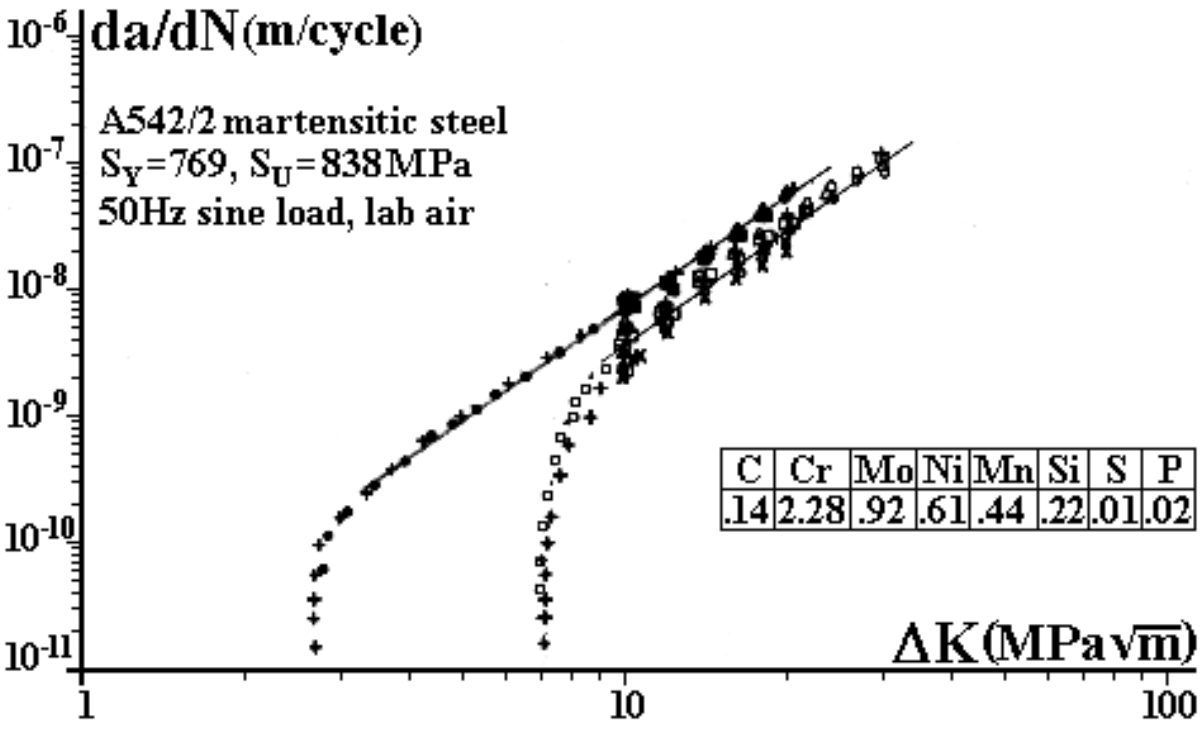

Figure 11: A542-2 (2.25Cr1Mo martensitic steel) **da/dN×ΔK** curves at **R = 0.05** and **R = 0.7**.

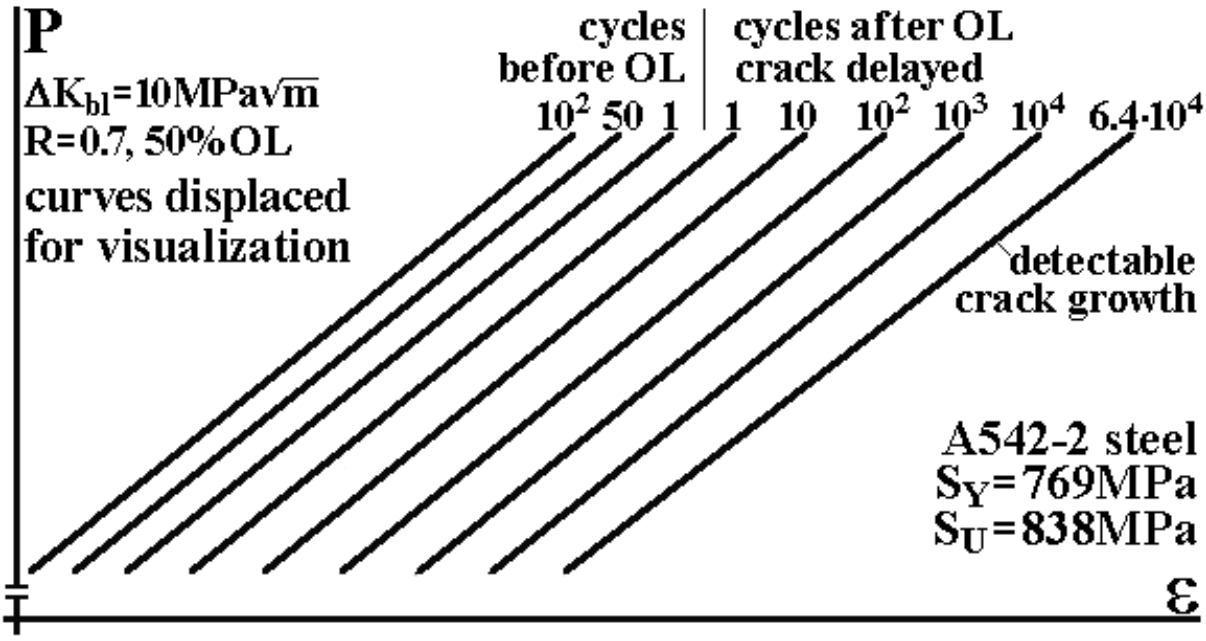

Figure 12: **P×ε** curves showing ***no*** closure neither before nor after the 50% OL that delayed this crack (the change in the **P×ε** slope after the crack restarted to grow reflects the measurement sensitivity)

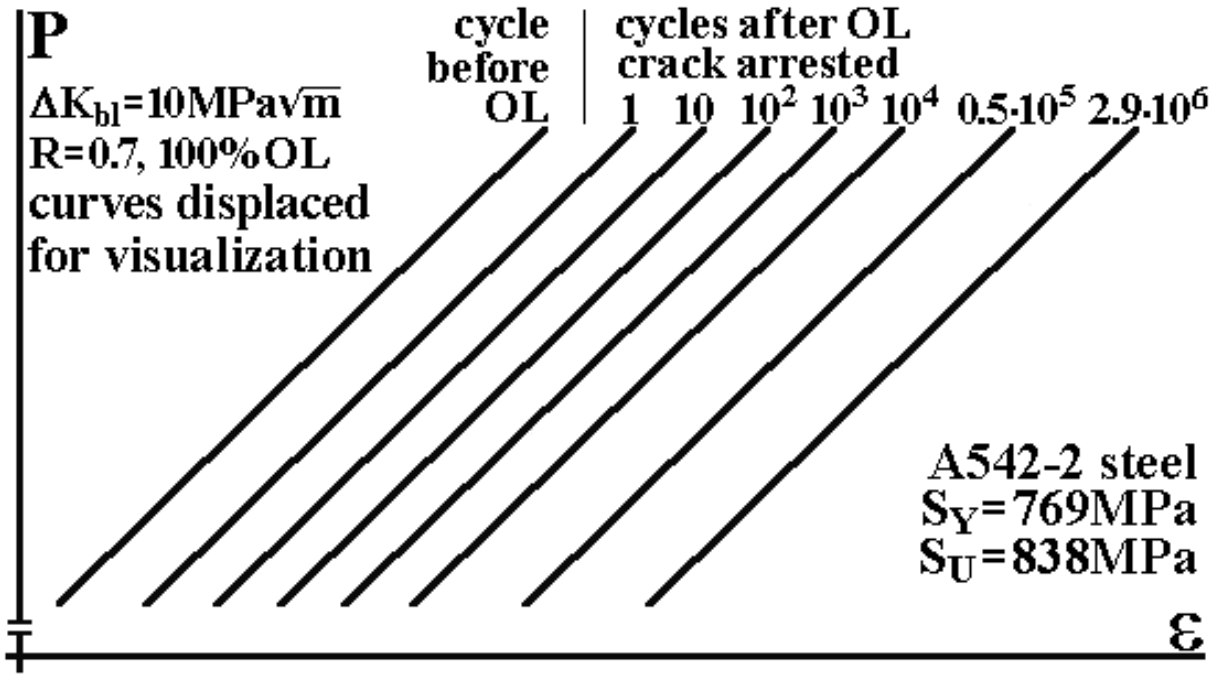

Figure 13: **P×ε** curves where ***no*** closure was detected, neither before nor after the overload in this crack arrest test after a single 100% OL, applied over a constant baseline load ΔK_{bl} = **10MPa√m** and **R = 0.7**.

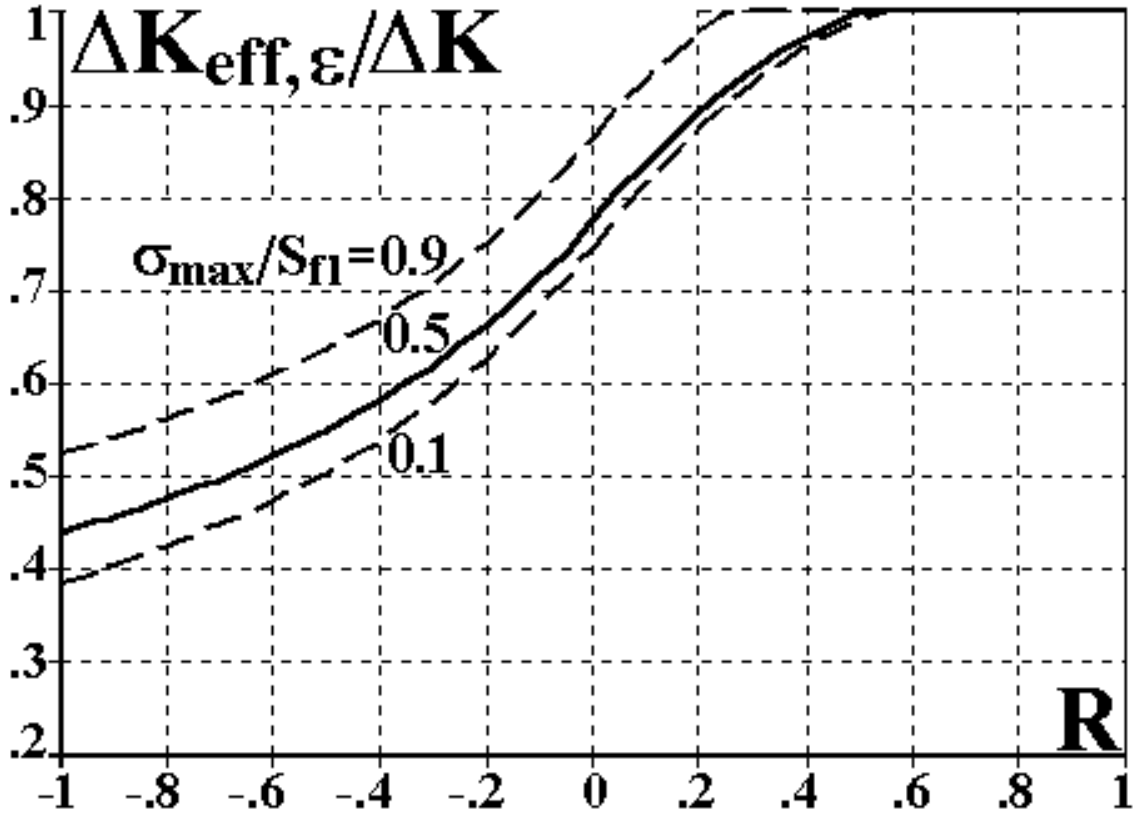

Figure 14: $\Delta K_{eff,\varepsilon}/\Delta K$ ratio predicted from Newman's FE closure model [16], indicating that no closure is expected for R-ratios higher than **R = 0.5** under CA loading.

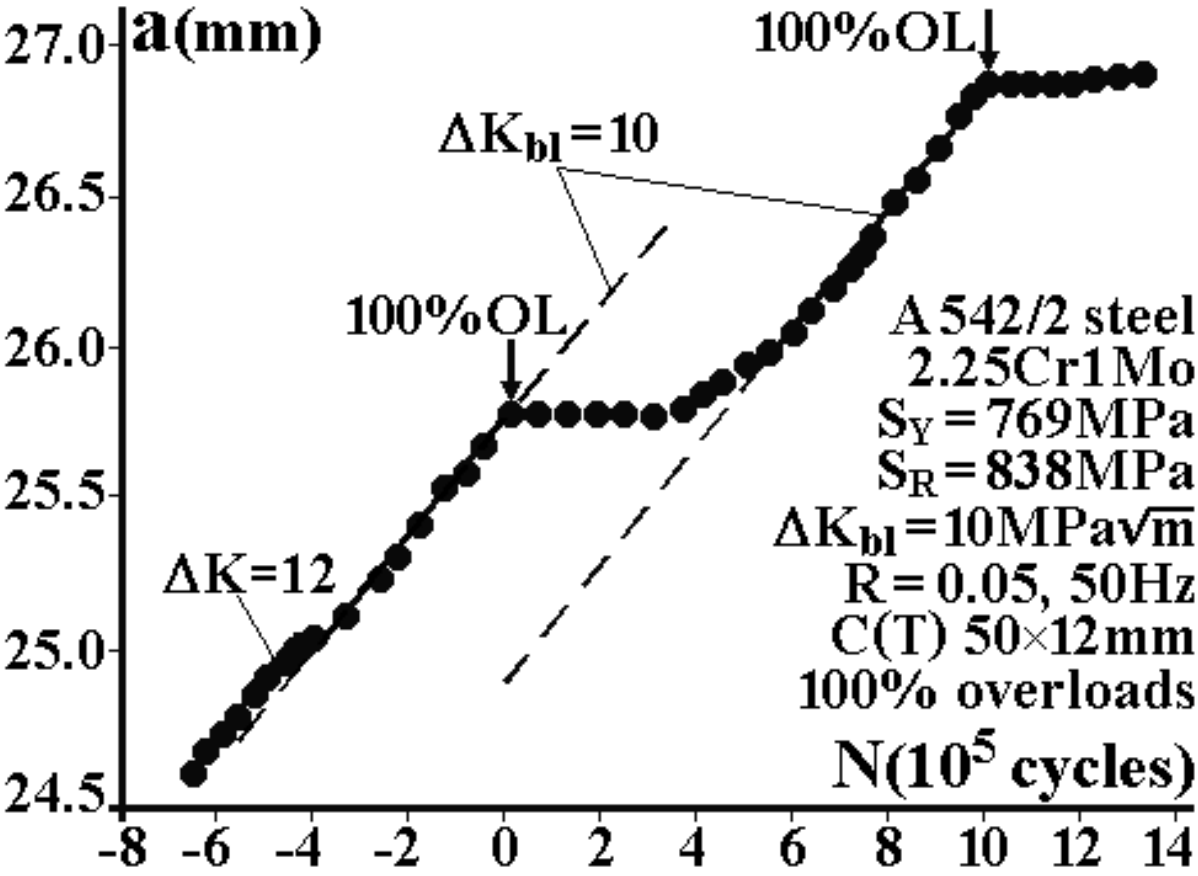

Figure 15: Fatigue crack growth retardation after **100%** overloads applied at a low **R = 0.05**, on a crack growing at a quasi-constant ΔK_{bl} **= 10MPa√m** under plane-ε conditions.

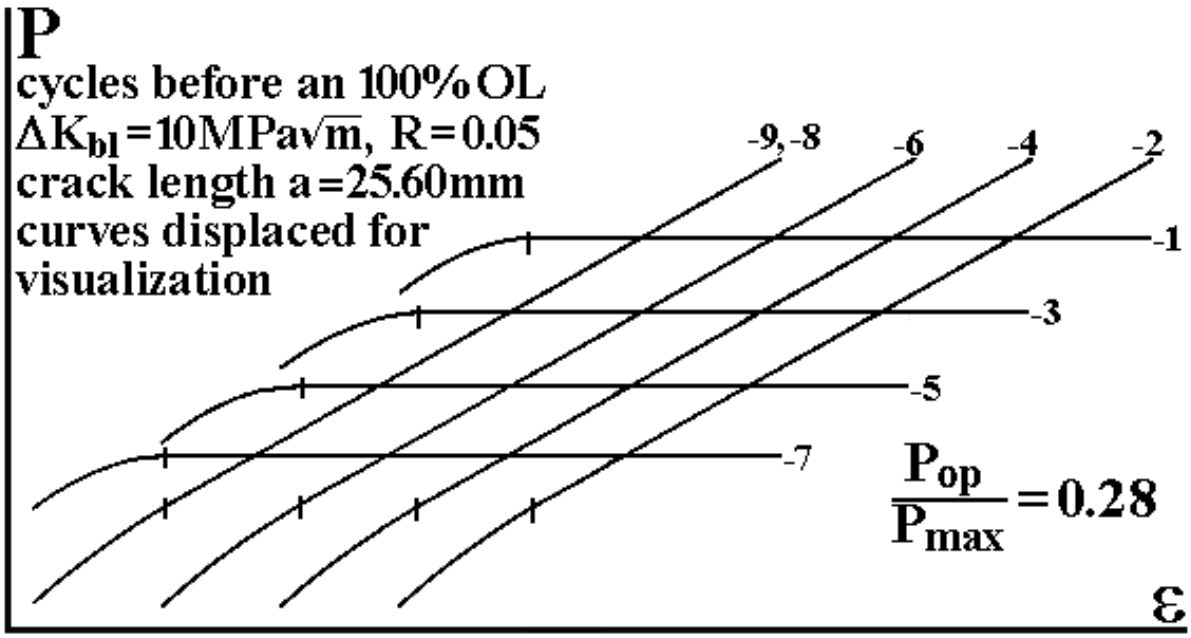

Figure 16: **P×ε** curves where crack closure was clearly measured in the 9 cycles before a 100% overload (−9 through −1) that retarded the subsequent fatigue crack growth, all with P_{op}/P_{max} **= 0.28**.

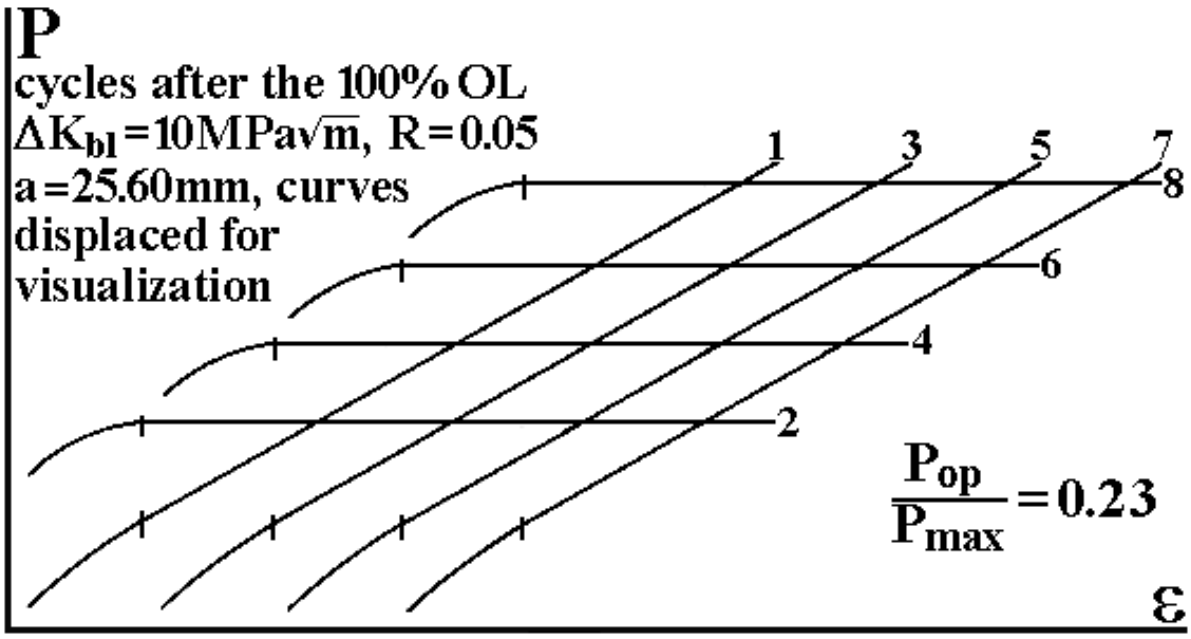

Figure 17: **P×ε** curves where significant crack closure also occurred just after the overload at a low **R = 0.05**, but the ratio $\mathbf{P_{op}/P_{max} = 0.23}$ was smaller than the $\mathbf{P_{op}/P_{max} = 0.28}$ measured before, indicating that $\mathbf{\Delta K_{eff}}$ ***increased*** due the overload in this case.

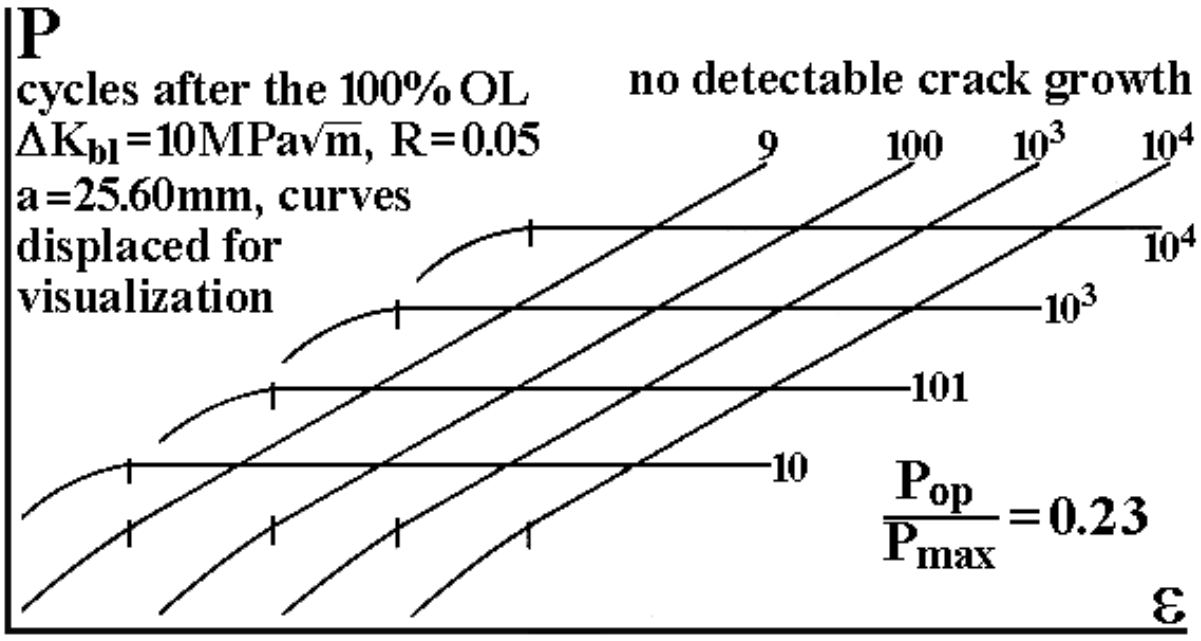

Figure 18: **P×ε** curves where no crack growth was detected during the next 10^4 cycles after the 100% overload, despite the **22%** ***increase*** in $\mathbf{\Delta K_{eff}}$ caused by it.

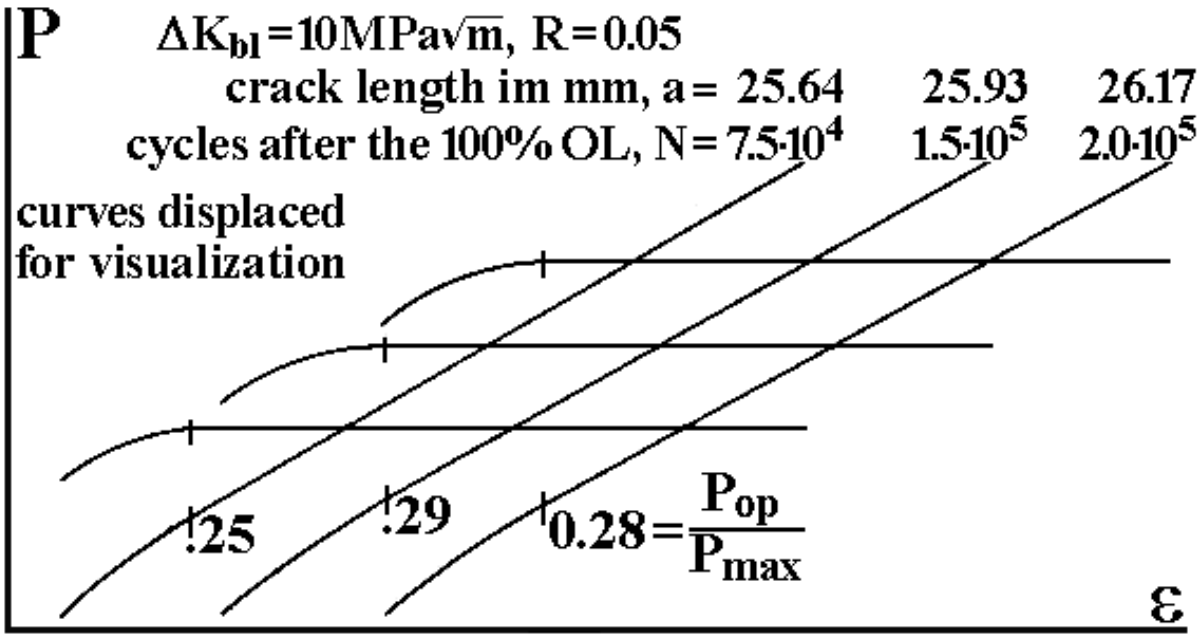

Figure 19: **P×ε** curves showing that at $7.5 \cdot 10^4$ cycles after the overload, when the crack growth could be detected again and the retardation started to diminish, the $\mathbf{P_{op}/P_{max}}$ ratio started to ***increase*** (causing $\mathbf{\Delta K_{eff}}$ to ***decrease***) until reaching its pre-overload $\mathbf{P_{op}/P_{max} = 0.28}$ value at $2.0 \cdot 10^5$ cycles after the OL, when its effect had almost disappeared.

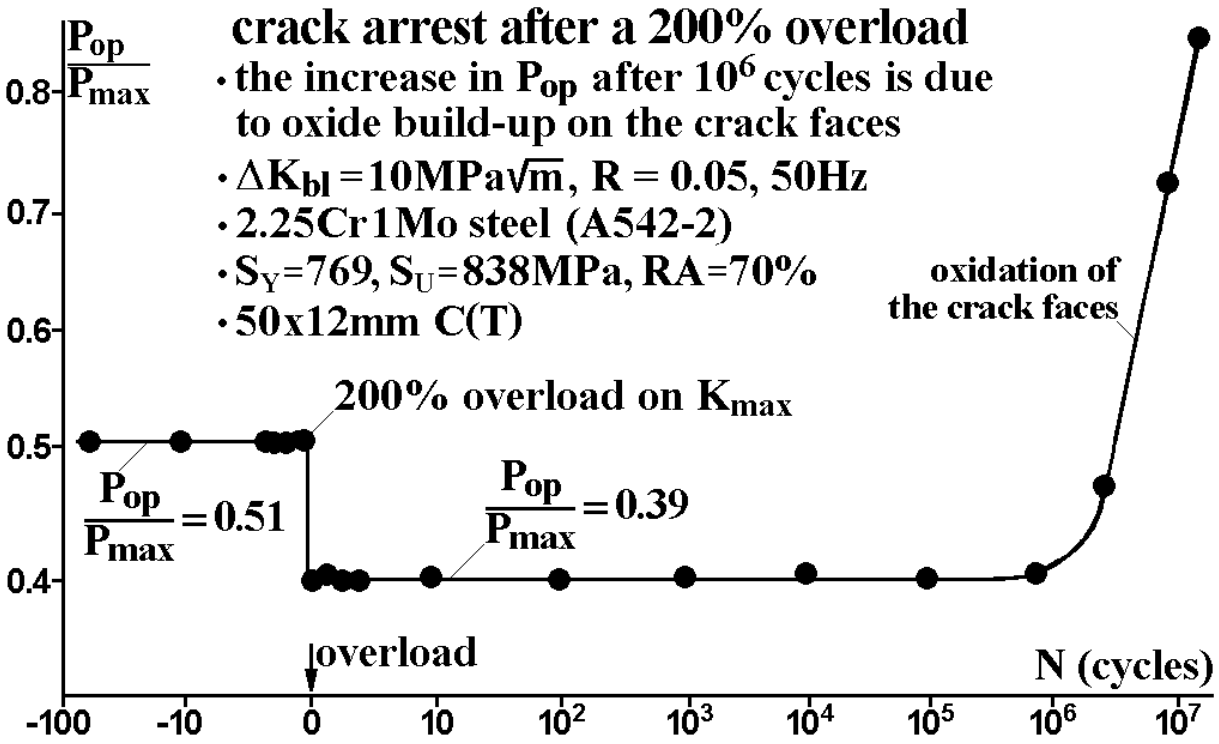

Figure 20: Crack ***arrest*** after a **200%** overload associated with a **31%** ***increase*** in $\mathbf{\Delta K_{eff}}$.

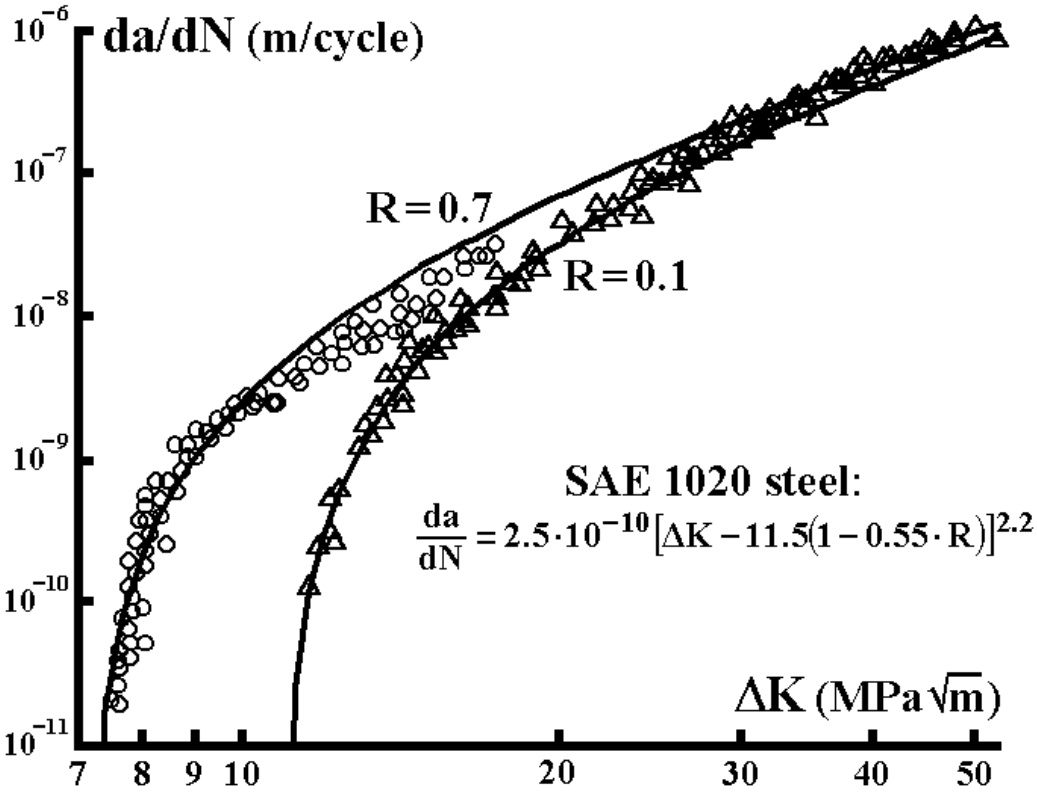

Figure 21: **da/dN** equation fitted to the SAE 1020 steel data.

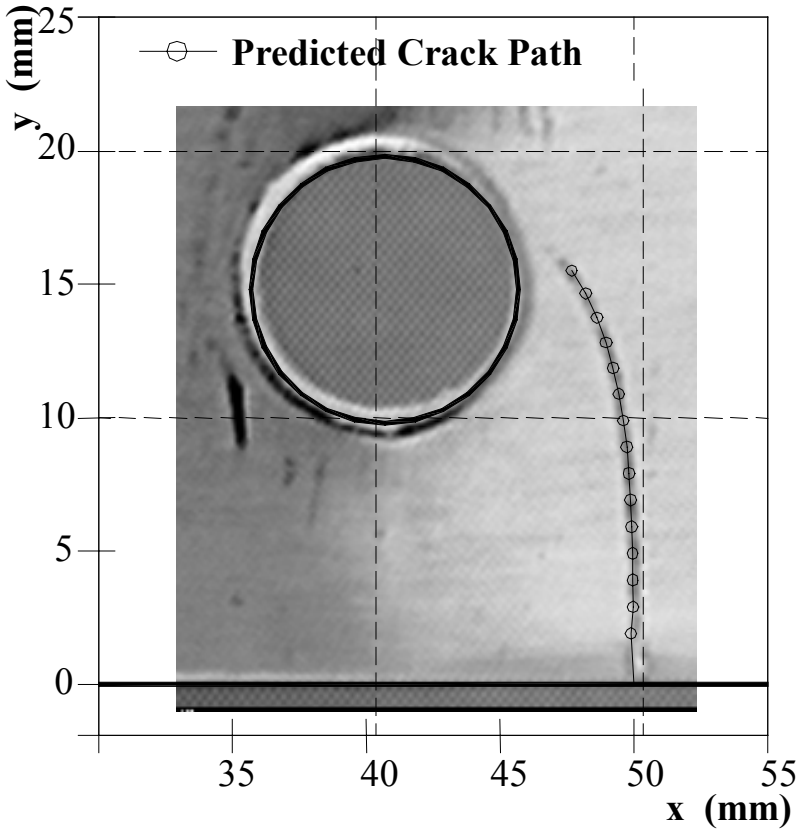

Figure 22: Predicted (dots) and measured paths of a fatigue crack propagated on a single edge notch 4 point bending SE(B) test specimen, modified with a hole machined on the left of the starting notch to curve the crack path.

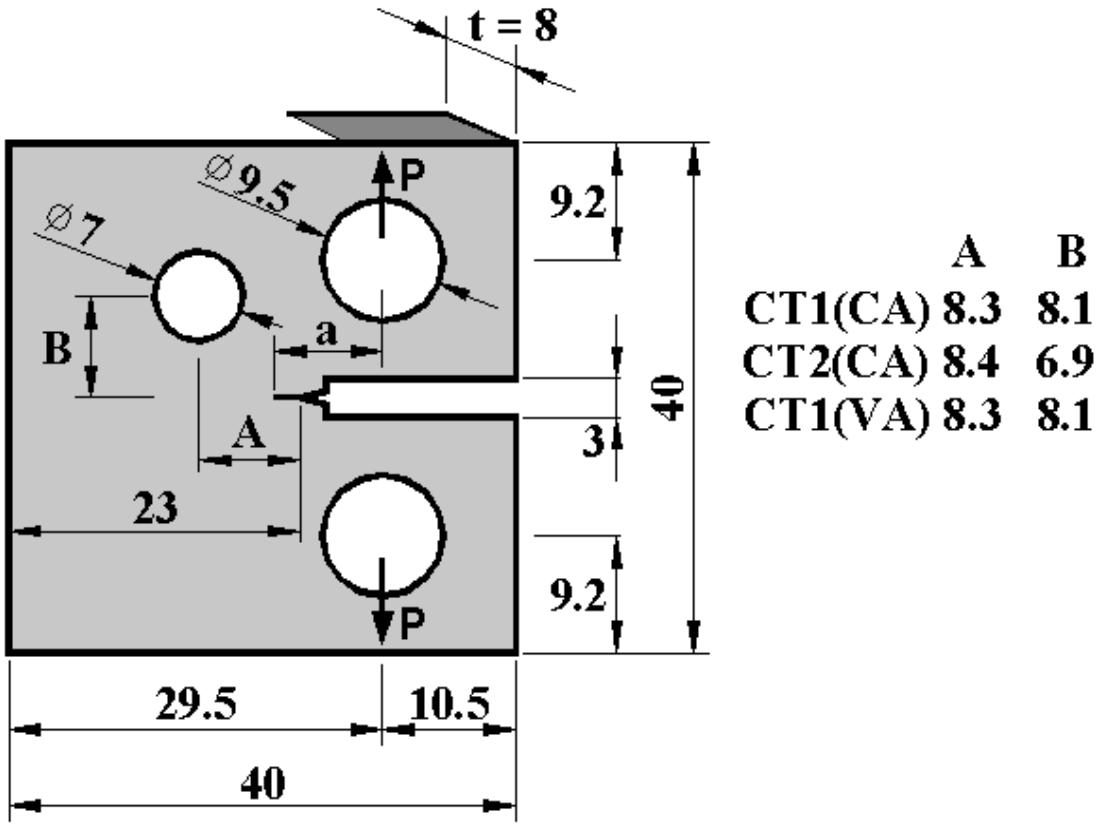

Figure 23: Measured dimensions of the hole-modified C(T) specimens (mm).

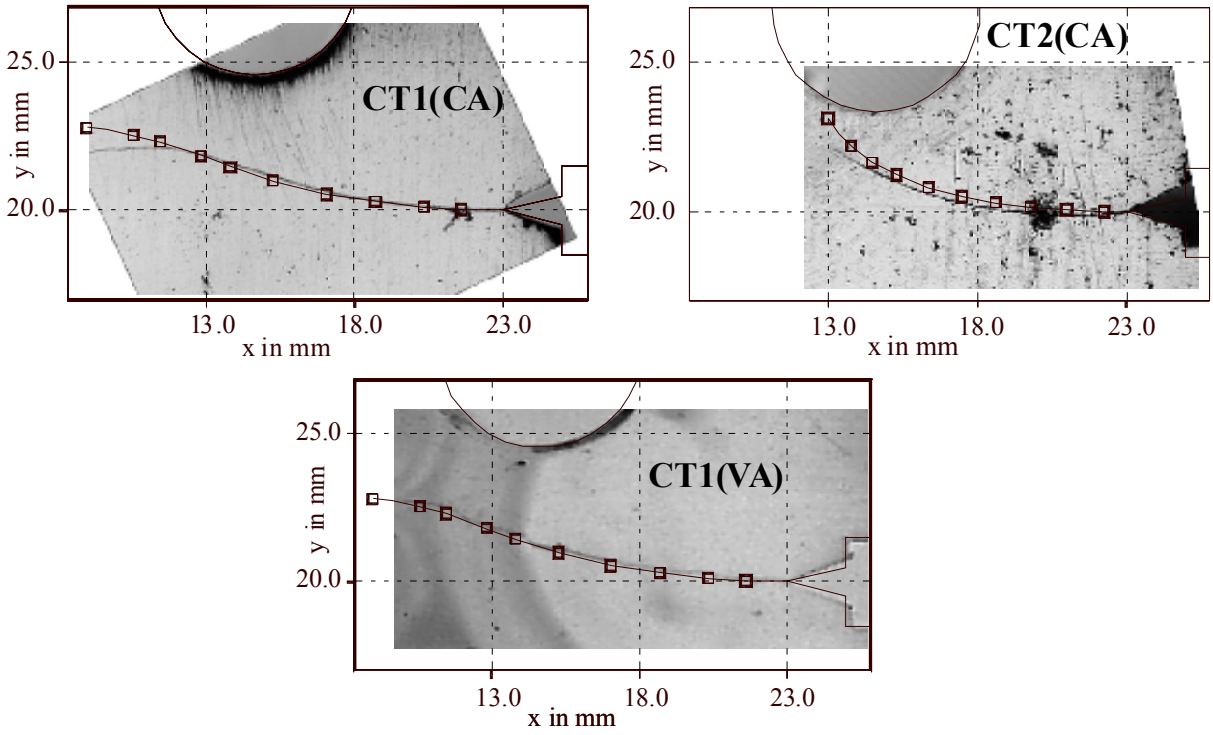

Figure 24: Predicted and measured crack paths for the modified C(T) specimens (mm).

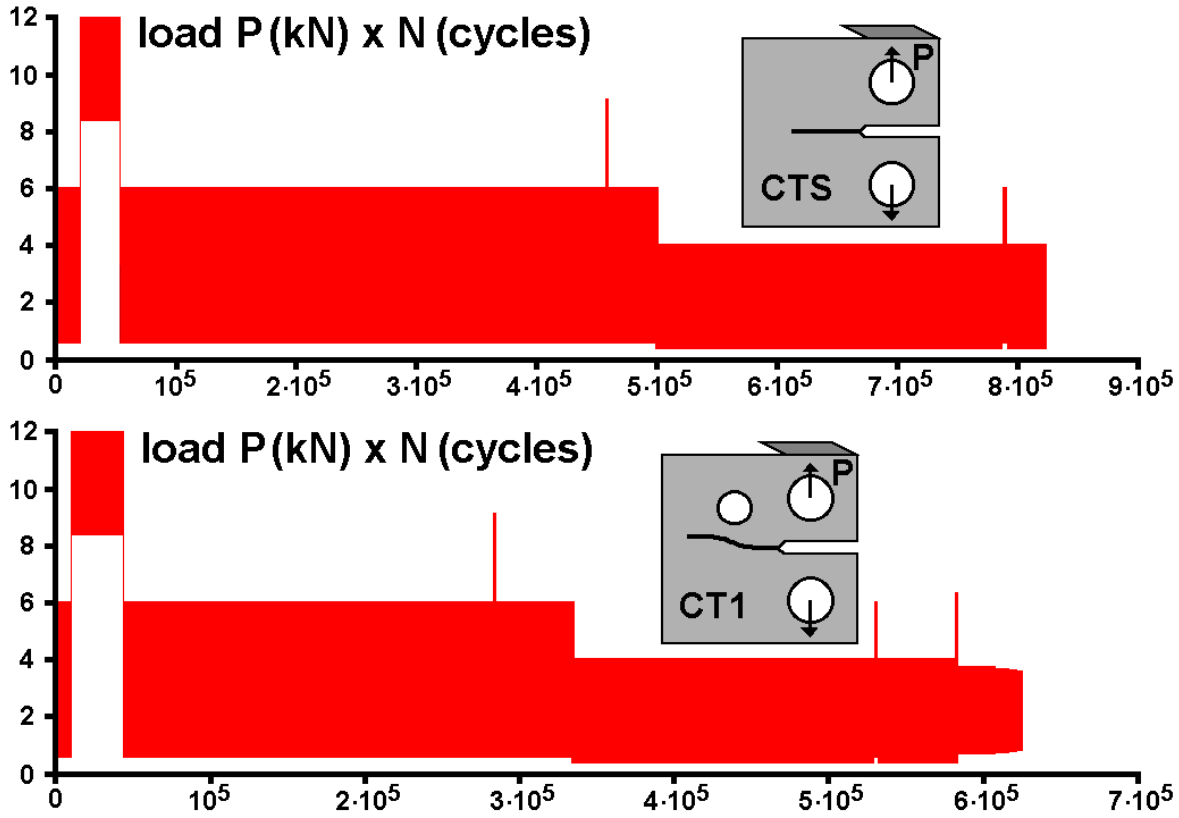

Figure 25: Applied load history (in kN) for the standard C(T) and for the modified CT1(VA) specimens.

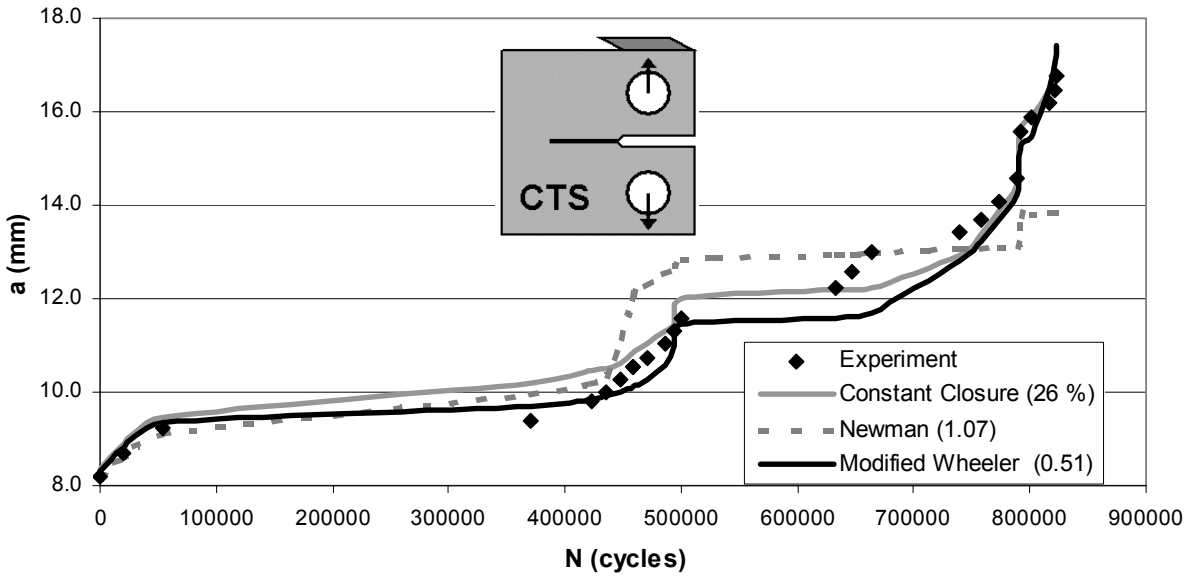

Figure 26: Measured crack sizes and results of the fitted load sequence effects engineering models on the standard C(T) tested under variable amplitude (VA) loading.

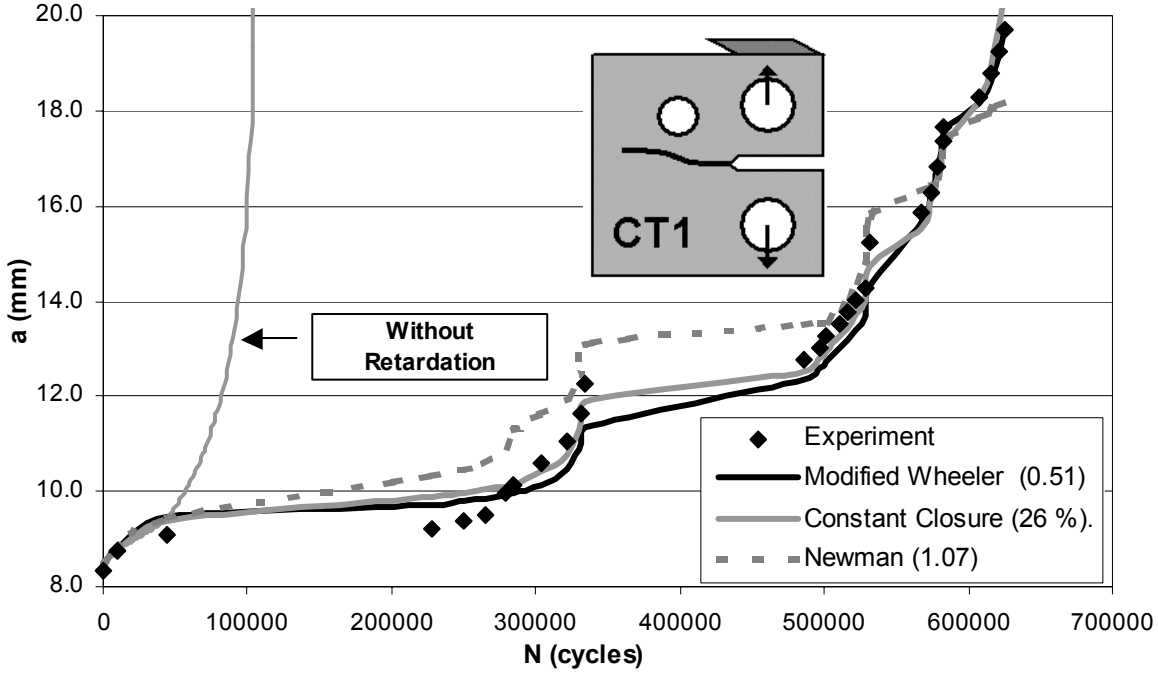

Figure 27: Crack growth predictions on the holed C(T) made by the several crack propagation models (with adjustable constants calibrated by testing the standard C(T) presented in Figure 26).

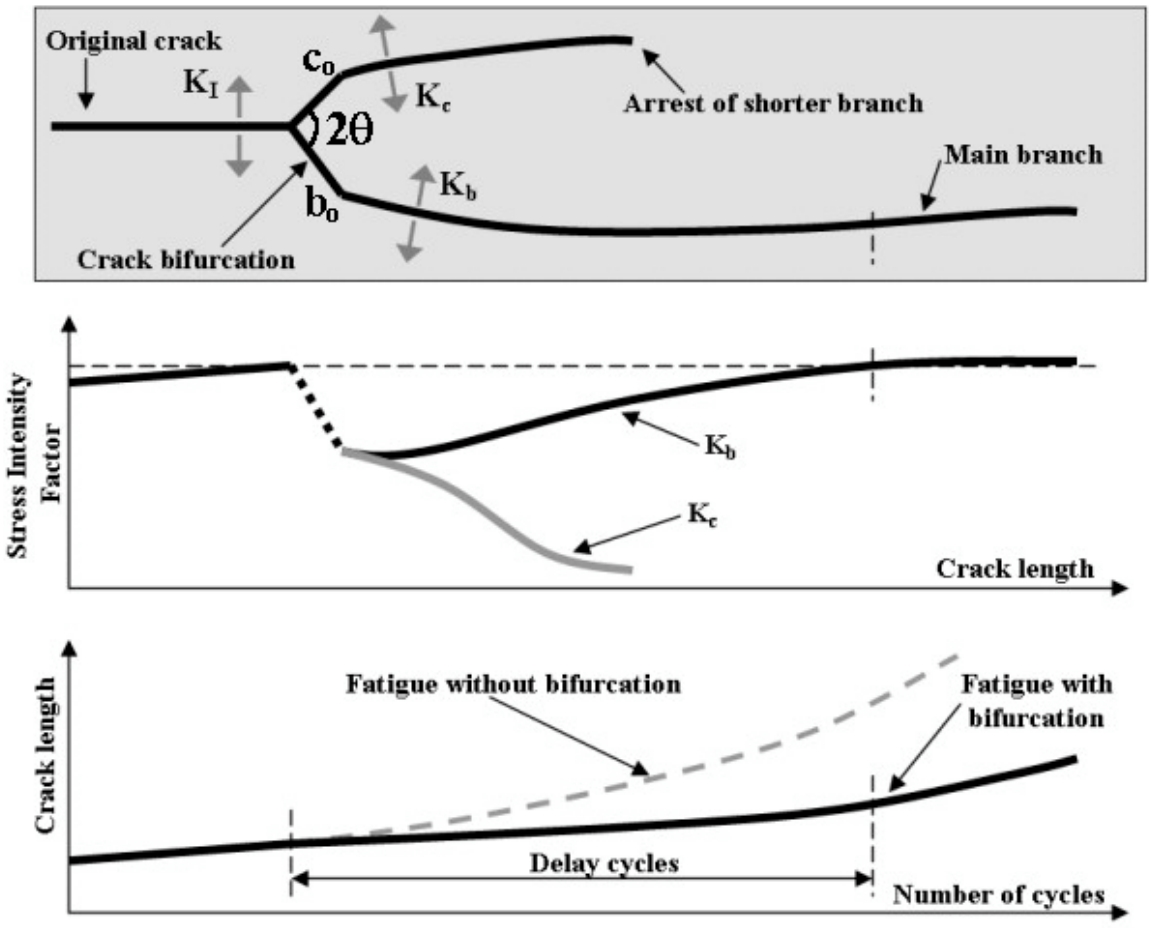

Figure 28: Typical propagation behavior of a bifurcated fatigue crack.

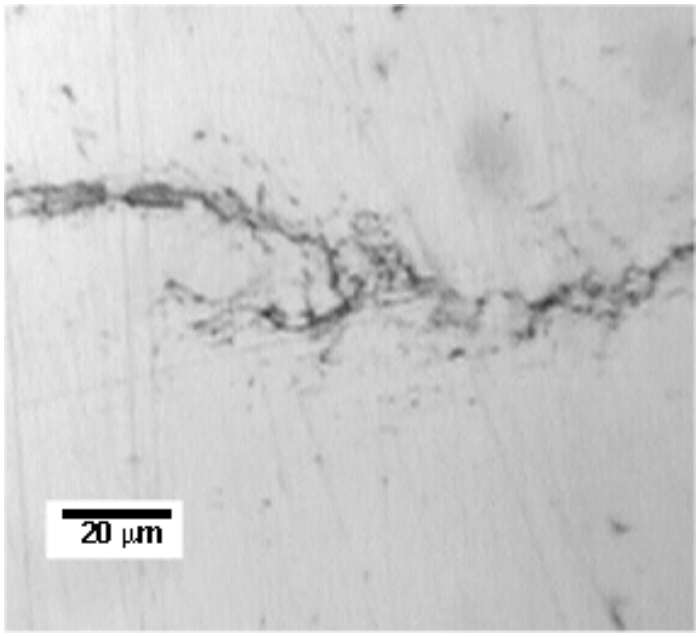

Figure 29: Crack branching after a 100% overload in an SAE 4340 SE(T) specimen for ΔK_{bl} = **16.2MPa√m** and **R = 0.05**. Note that the shorter branch stopped, while the longer one continued to propagate to the left.

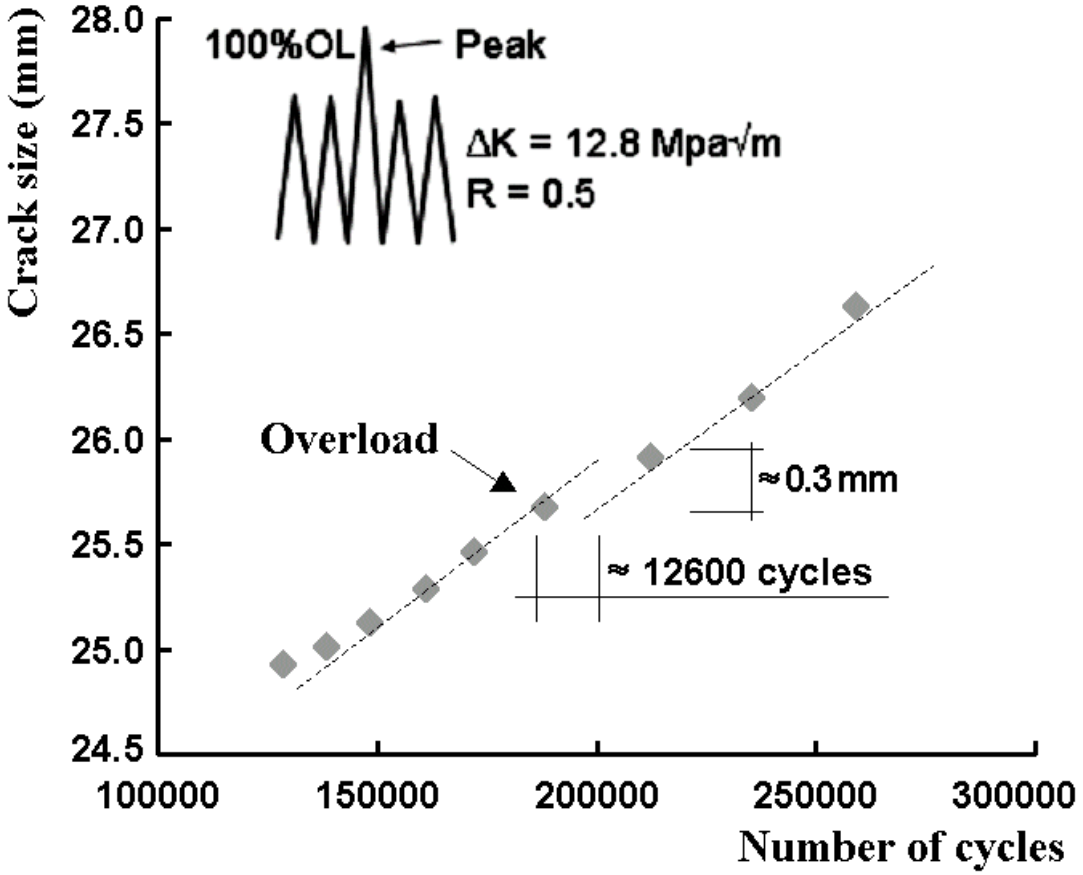

Figure 30: Fatigue crack growth retardation induced by a 100 % overload that caused crack branching in another SAE 4340 SE(T) specimen for ΔK_{bl} = **12.8MPa√m** and **R = 0.5**.

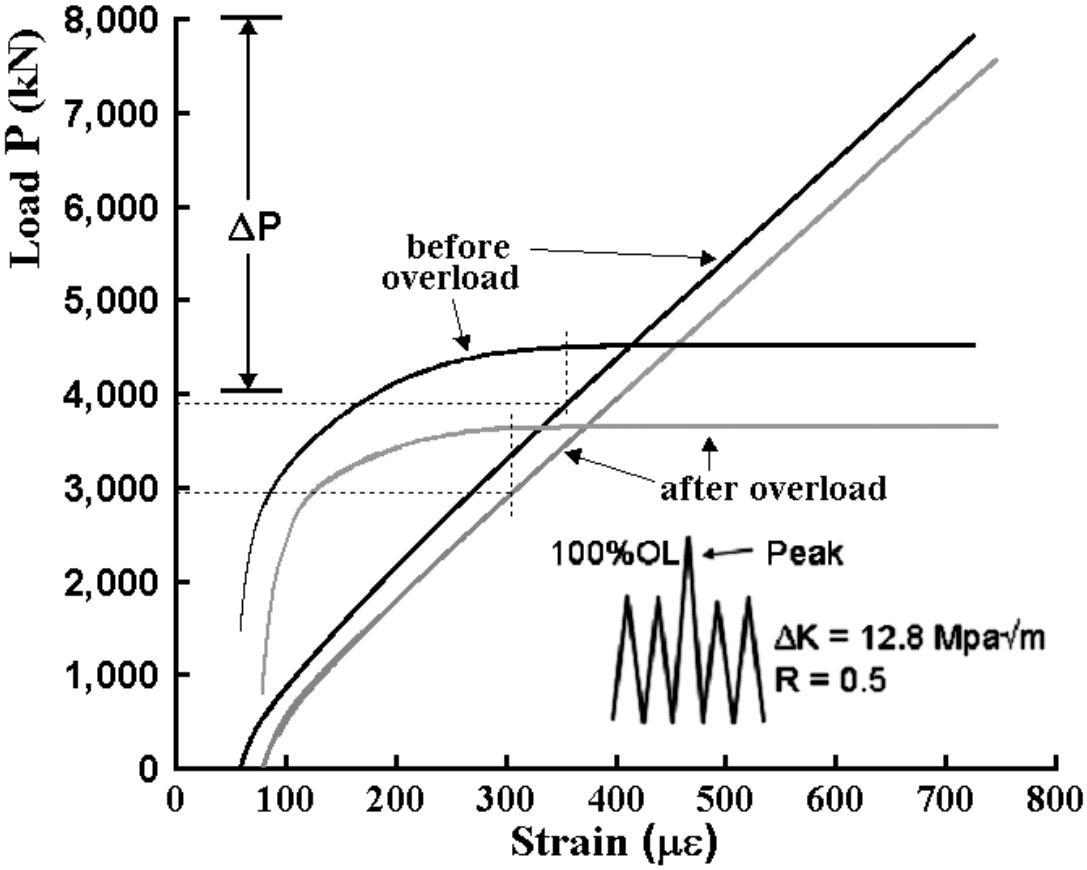

Figure 31: Opening load measurements, including the linearity subtractor output to enhance the non-linear part of the load versus back face strain ε, made before and after the overload test reported in Figure 30.

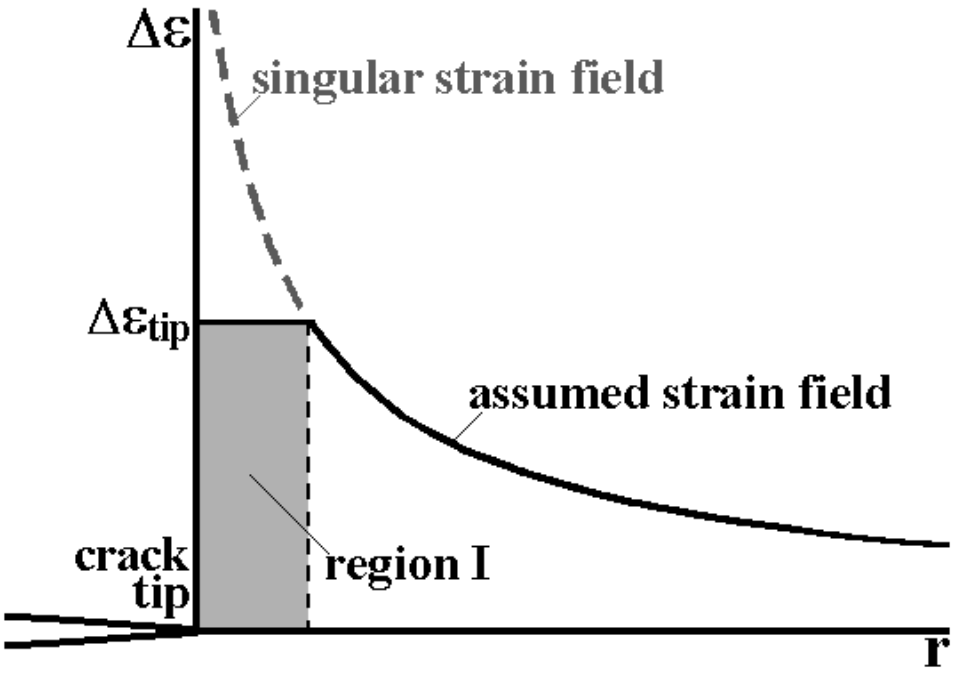

Figure 32: Estimated (solid line) non-singular strain distribution ahead of a real (blunt) crack tip, which has a small but a certainly not zero radius, limiting the HRR field by the strain range at the crack tip $\Delta\varepsilon_{tip}$, calculated by a strain concentration rule.

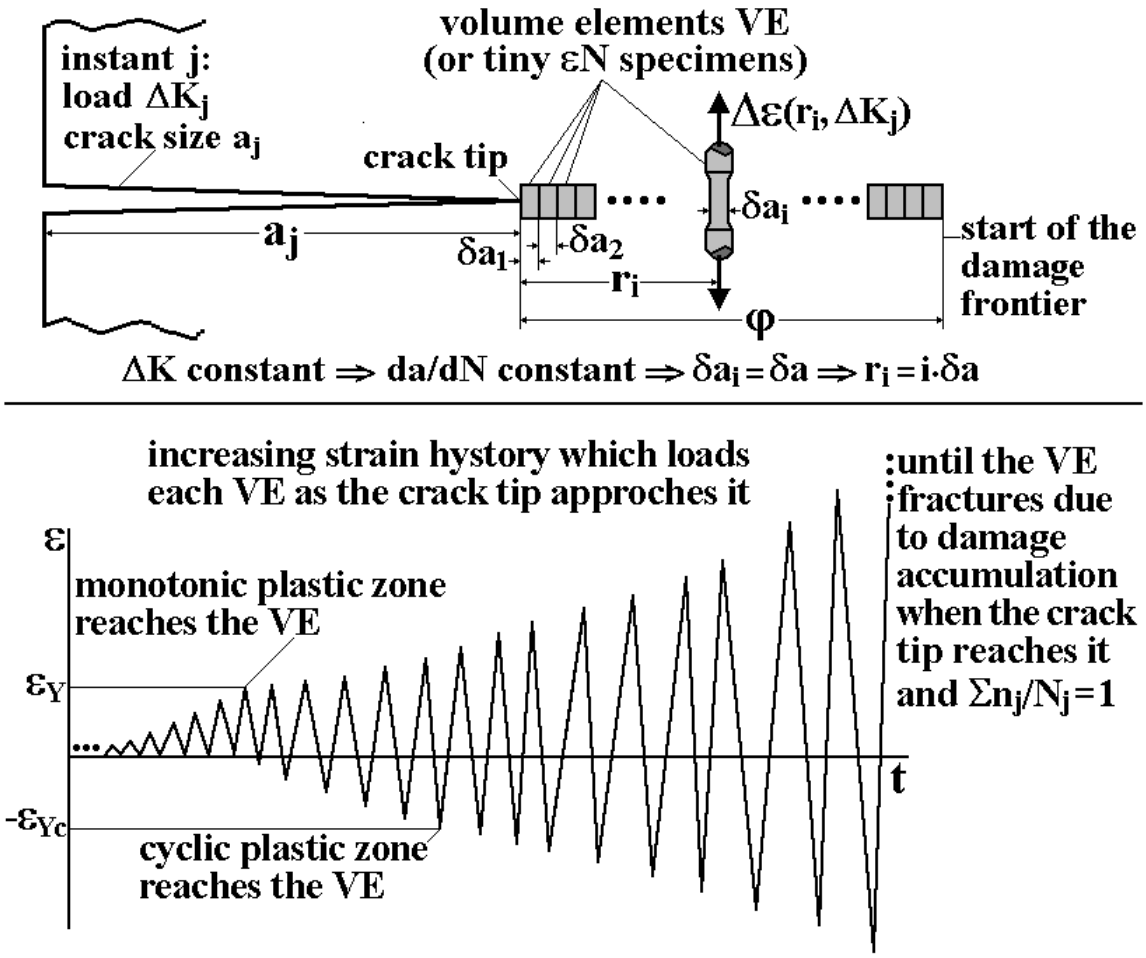

Figure 33: Schematics of the fatigue crack growth behavior, assumed to be caused by the sequential fracture of volume elements (or tiny **εN** specimens) at every load cycle, loaded by an increasing strain history as the crack tip approaches them.

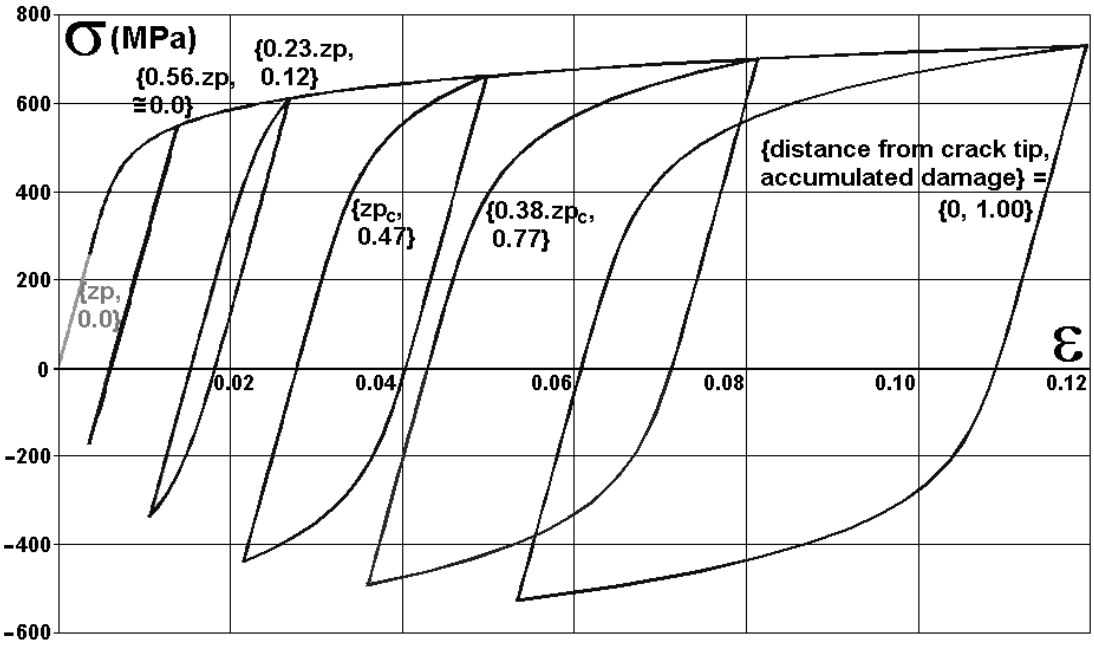

Figure 34: Schematics of the hysteresis loops at a fixed VE at different crack growth stages, under constant **ΔK** loading, showing that an accumulated damage of 0.47 is already present in this VE when it is reached by the cyclic plastic zone $\mathbf{zp_c}$.

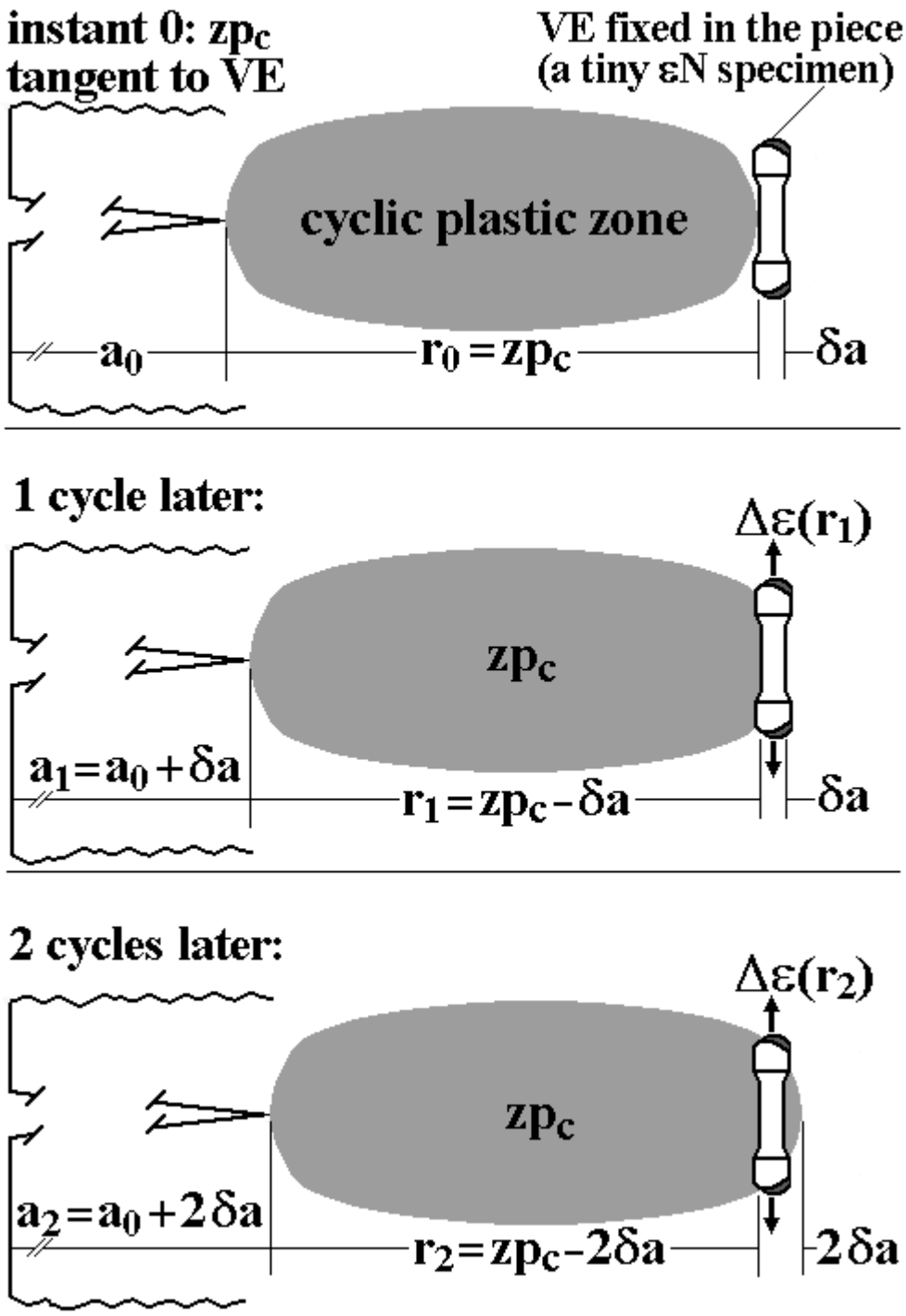

Figure 35: Schematics of the increasing strain ranges in any given VE as the crack grows and its tip approaches the VE.

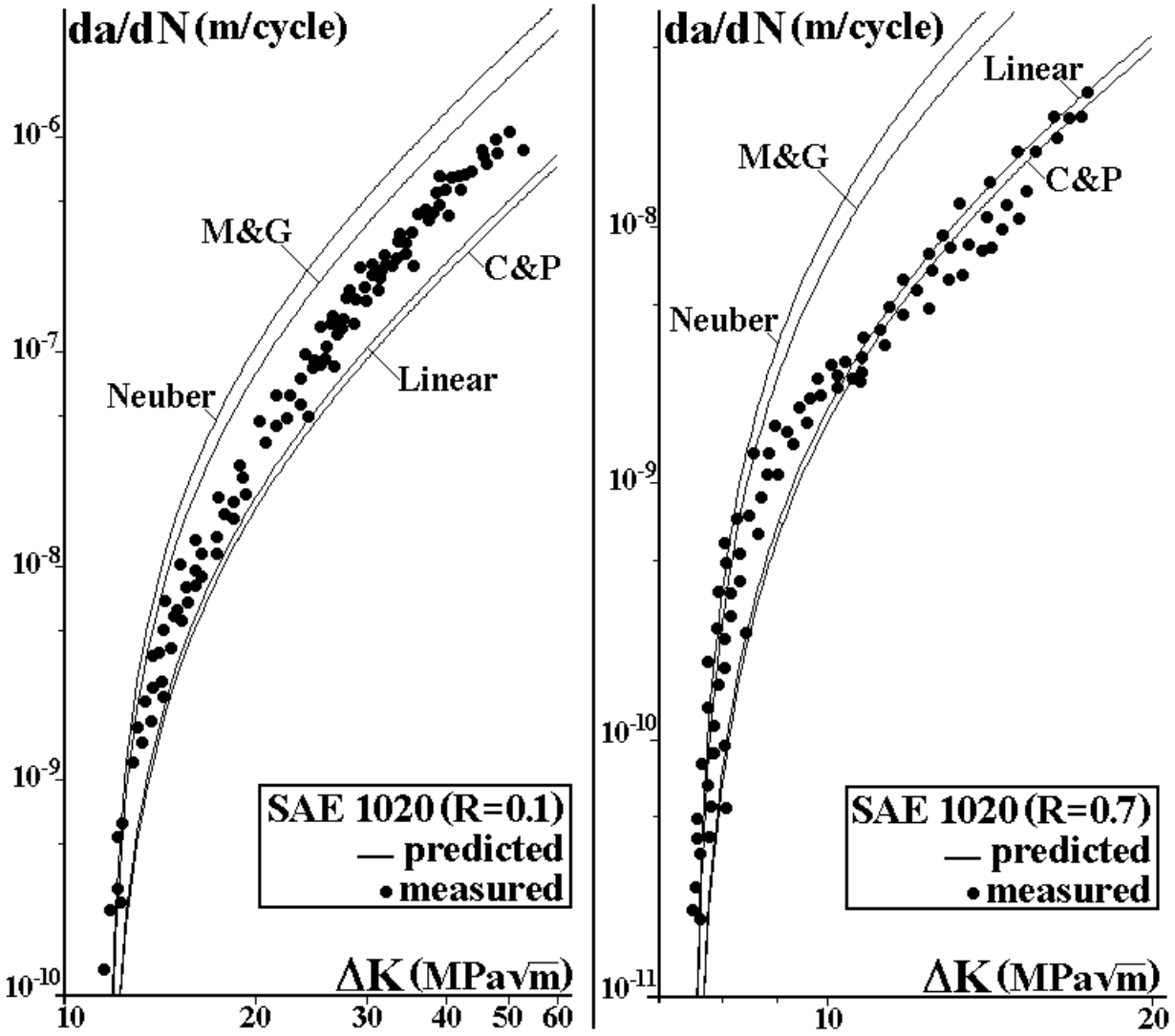

Figure 36: **da/dN×ΔK** behavior measured and ***predicted*** by the various strain concentration rules used in the critical damage model, for SAE 1020 low carbon steel at **R = 0.1** and **R = 0.7**. (P&C = Paris and Creager, M&G = Molsky and Glinka.)

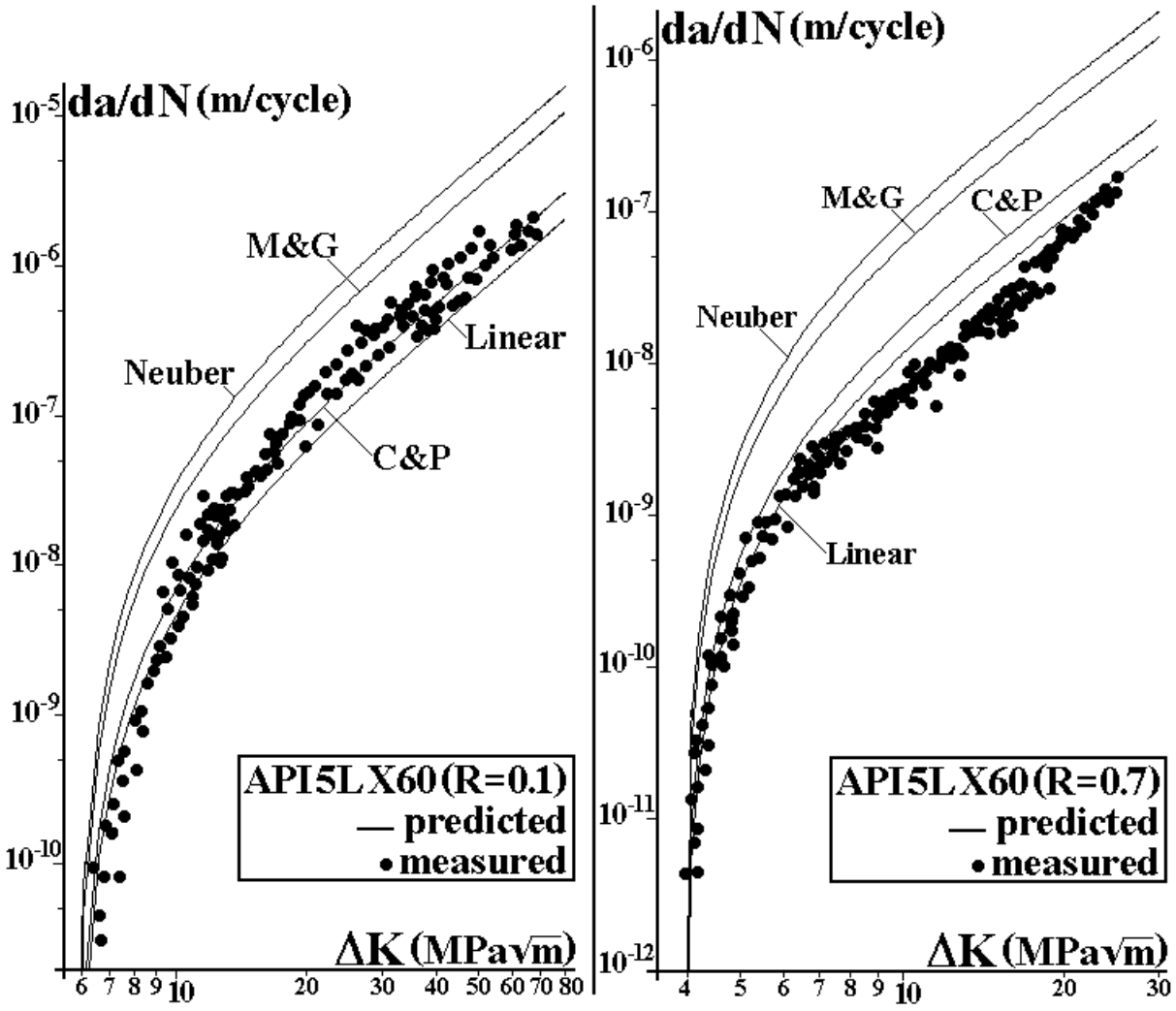

Figure 37: **da/dN×ΔK** behavior measured and ***predicted*** by the various strain concentration rules used in the critical damage model, for API-5L-X60 pipeline steel at **R = 0.1** and **R = 0.7**.

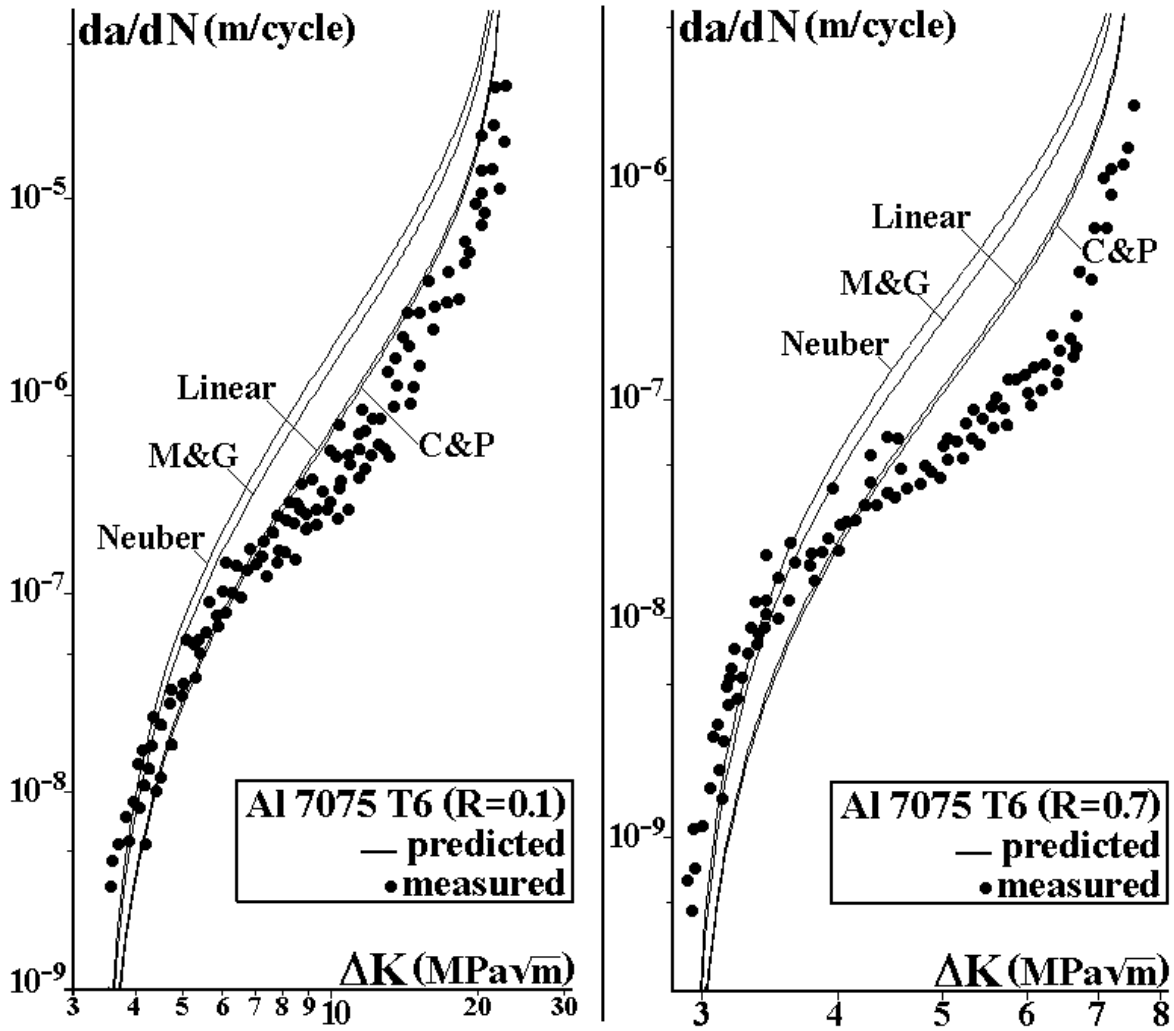

Figure 38: **da/dN×ΔK** behavior measured and ***predicted*** by the various strain concentration rules used in the critical damage model, for 7075 T6 high strength aluminum alloy at **R = 0.1** and **R = 0.7**.

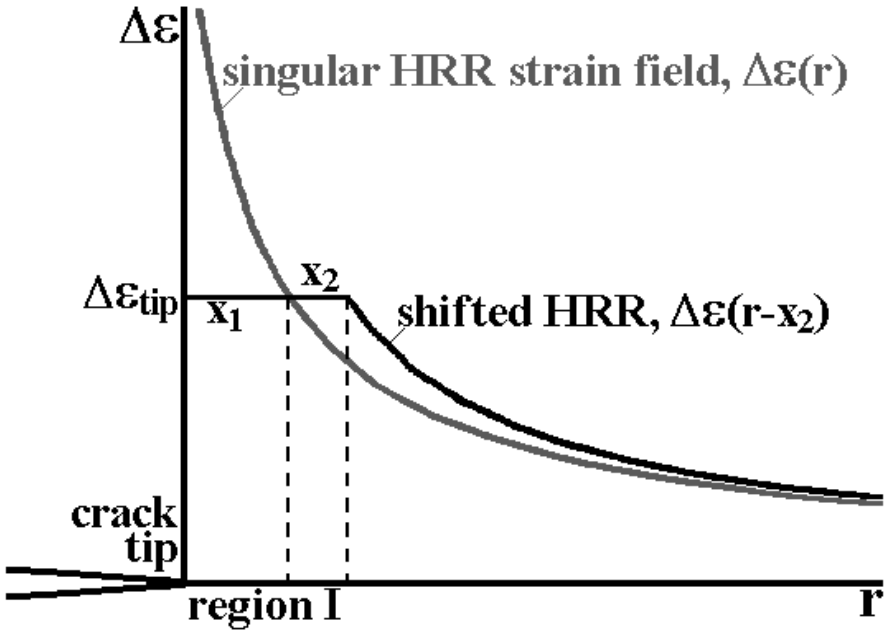

Figure 39: Singular and shifted HRR strain distributions ahead of the crack tip, limited by $\Delta\varepsilon_{tip}$.

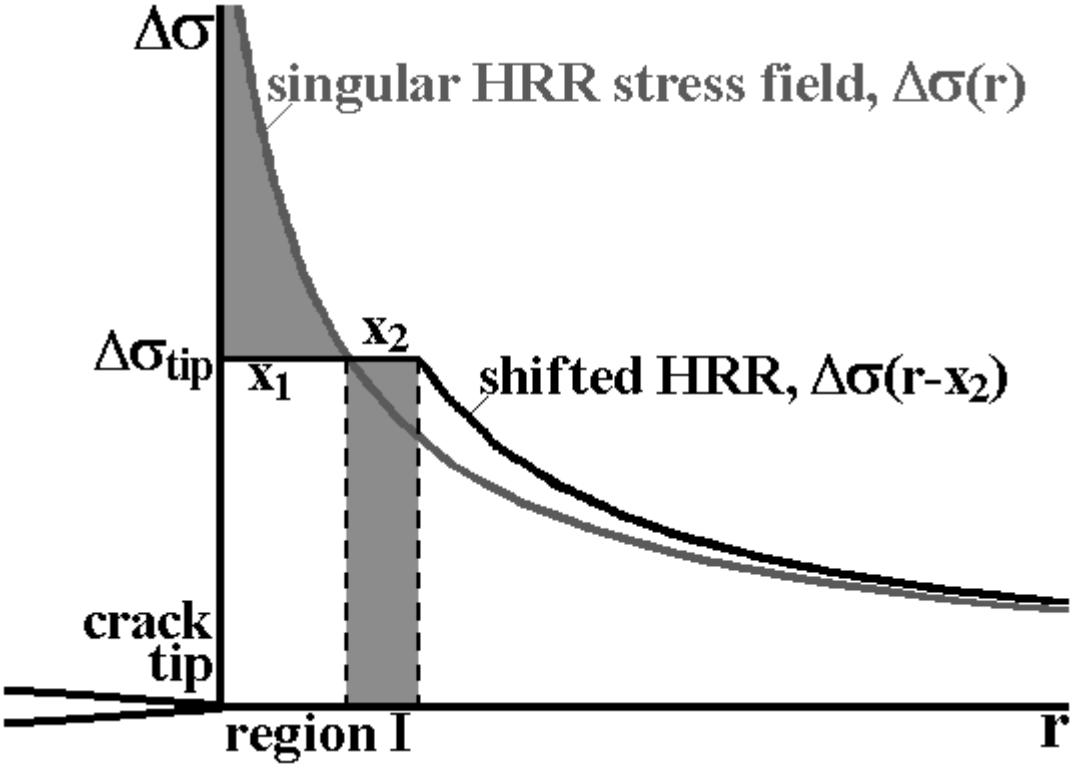

Figure 40: Singular and shifted HRR stress distributions ahead of the crack tip, limited by $\Delta\sigma_{tip}$, with the shadowed areas equalized to maintain equilibrium.

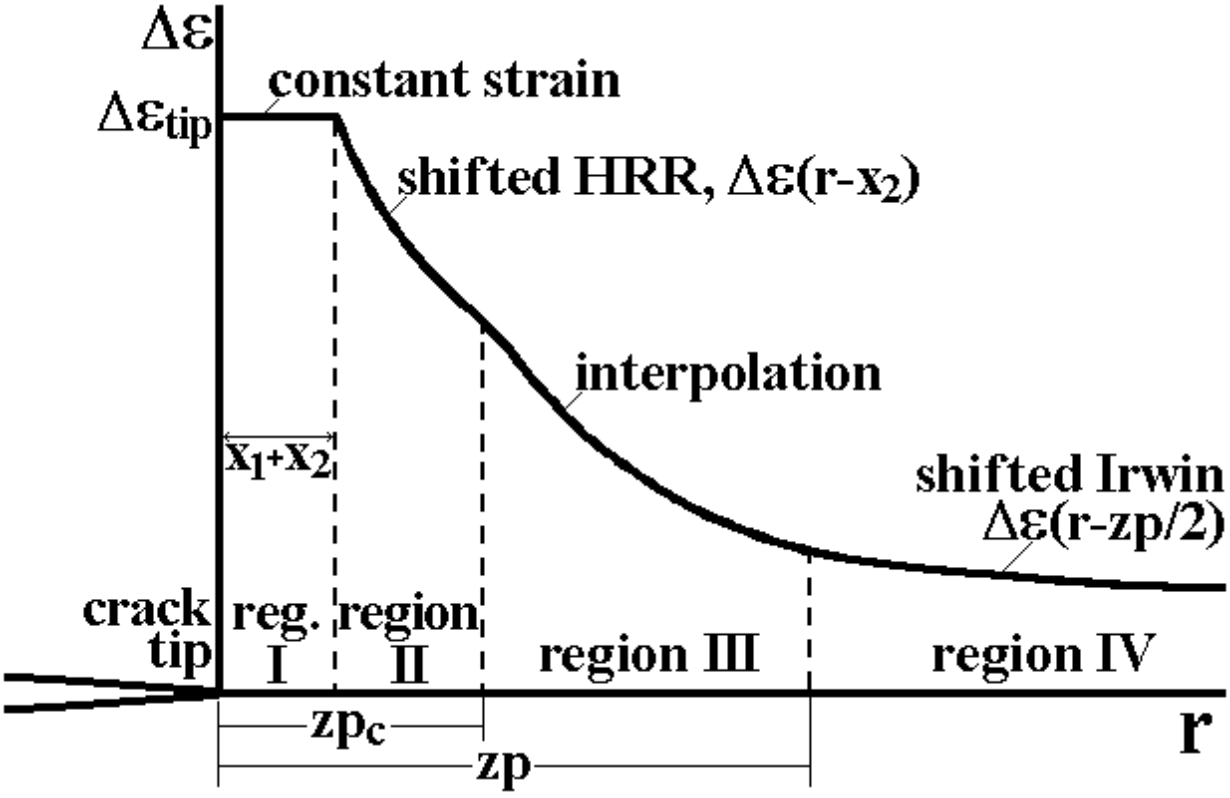

Figure 41: Proposed strain range distribution, divided in 4 regions to consider both the elastic and the plastic contributions to the damage ahead of the crack tip.

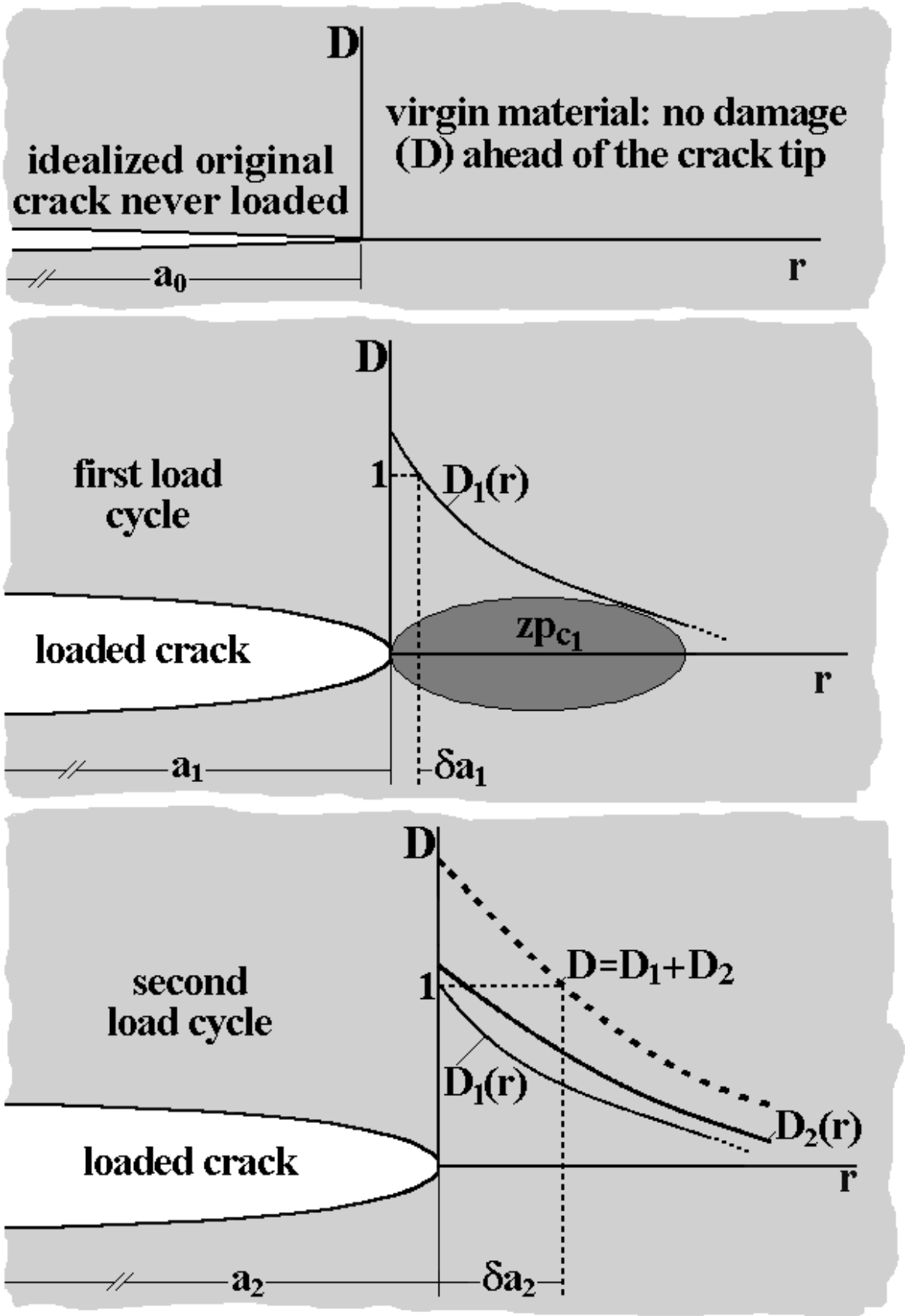

Figure 42: Schematics of the critical damage calculations, which under variable amplitude loading recognize variable crack increments by forcing the crack to grow over the region where **D = 1**.

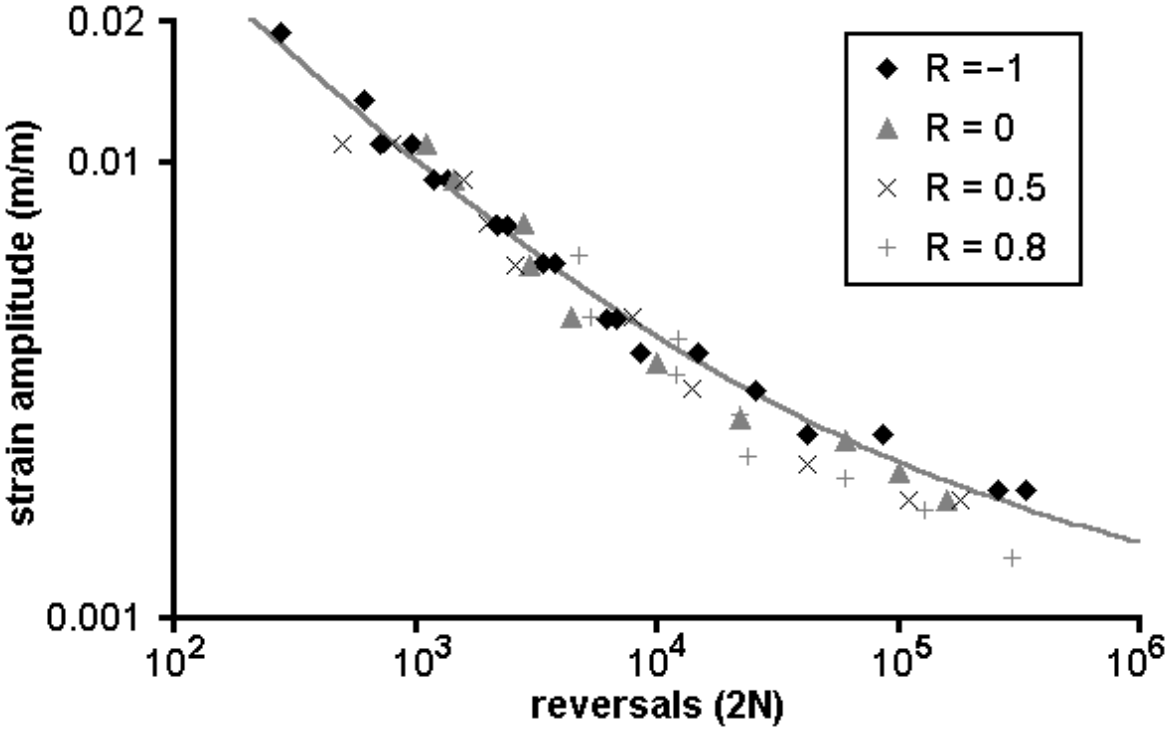

Figure 43: Measured strain-life data for the API 5L X52 steel, and Morrow elastic model that best fitted this data.

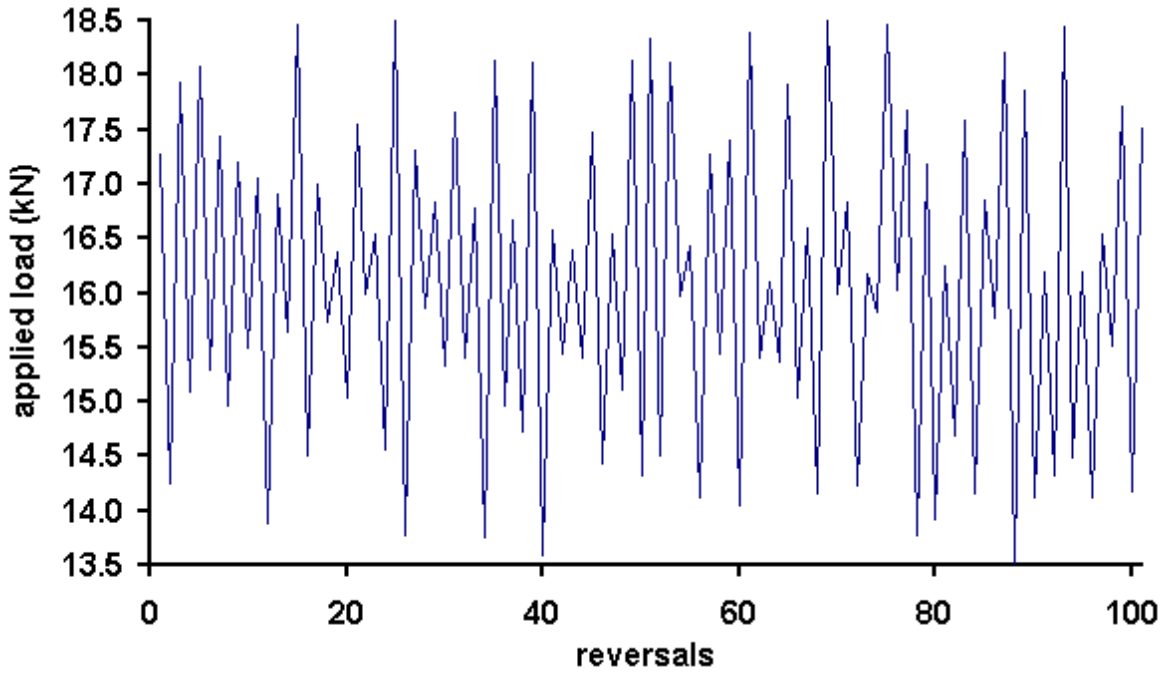

Figure 44: Variable amplitude load block applied to the API-5L-X52 steel C(T). Note the high mean R-ratio.

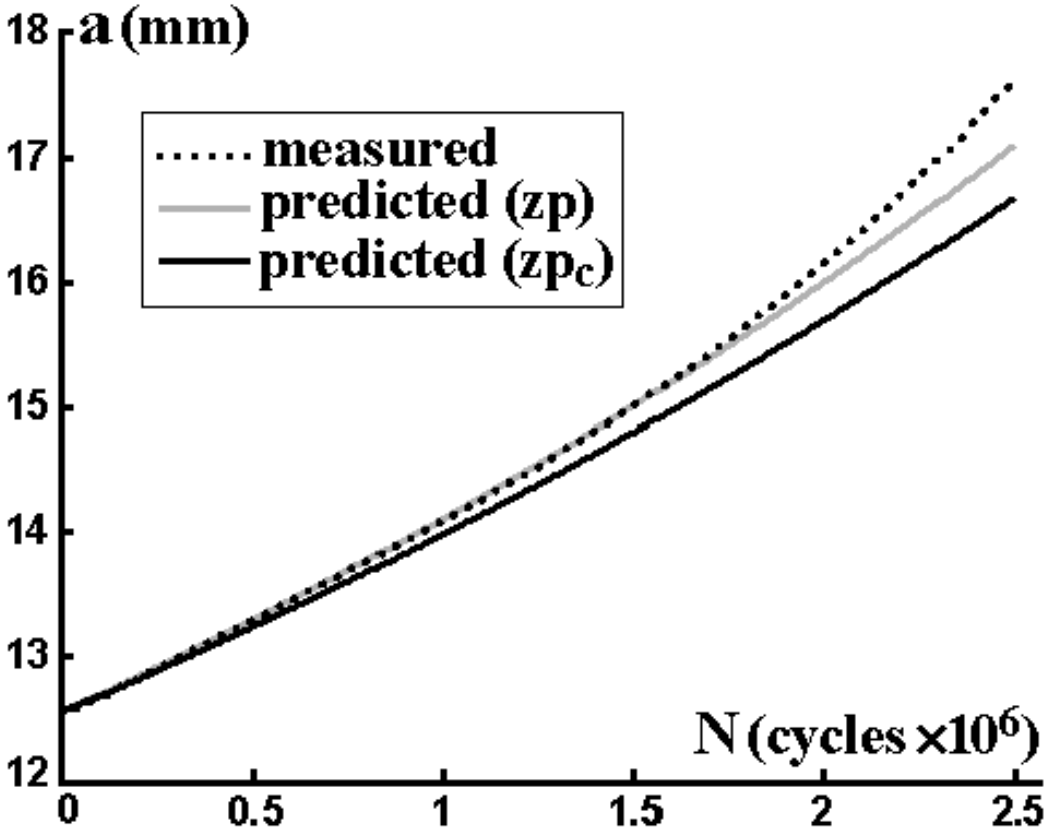

Figure 45: Comparison between the crack growth measurements and the εN-based predictions for the variable amplitude load presented in Figure 44 (API-5L-X52 steel).

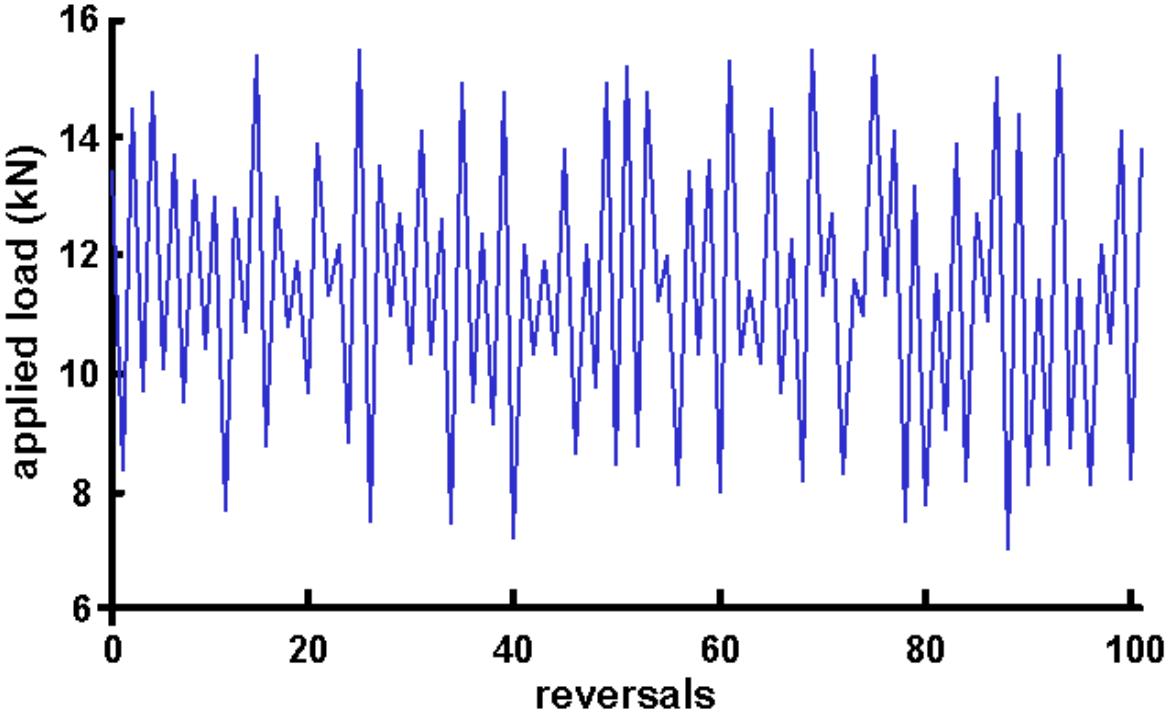

Figure 46: Variable amplitude load block applied to the SAE 1020 steel C(T). Again a high mean R-ratio was used in this test, to avoid the interference of possible significant closure effects which could mask the model performance.

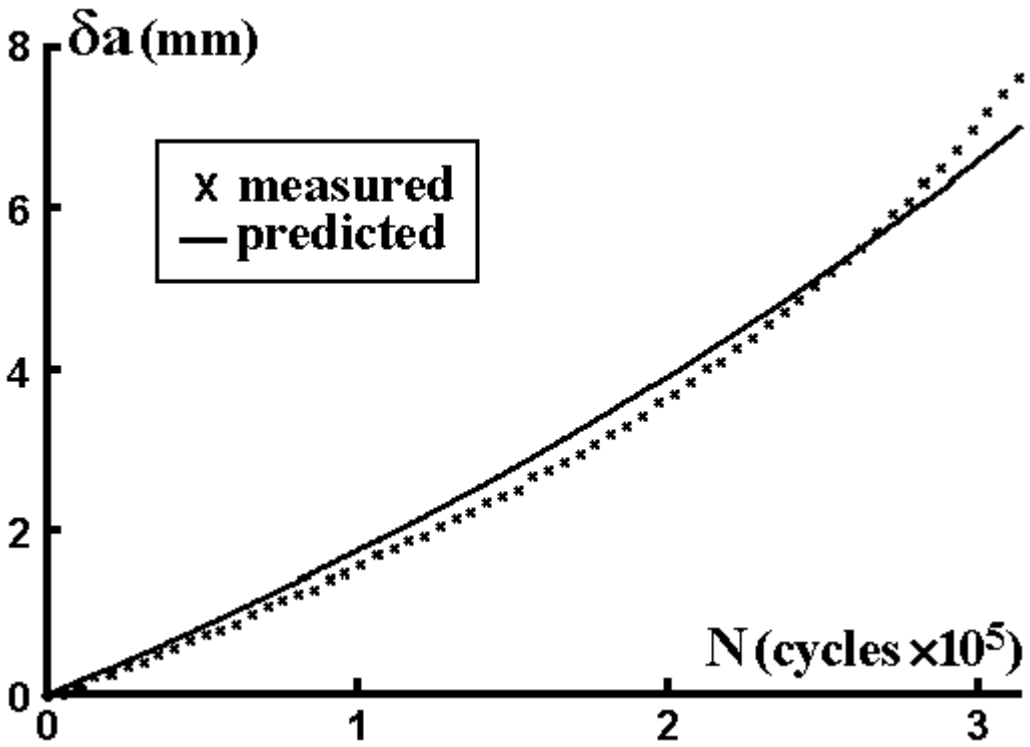

Figure 47: Comparison between the crack growth measurements and the εN-based predictions for the variable amplitude load presented in Figure 46 (SAE 1020 steel).